Science of the Total Environment 1034 (2026) 181849

Contents lists available at ScienceDirect

Science of the Total Environment

journal homepage: www.elsevier.com/locate/scitotenv

Probabilistic methane source attribution in Greater Accra: A hierarchical Bayesian dual-isotope approach

Ebenezer Aquisman Asare [a,*], Dickson Abdul-Wahab [b]

[a] Nuclear Chemistry and Environmental Research Centre, National Nuclear Research Institute (NNRI), Ghana Atomic Energy Commission (GAEC), Box LG 80, Legon-Accra, Ghana
[b] Department of Nuclear Science and Applications, School of Nuclear and Allied Sciences, University of Ghana, Atomic-Kwabenya, Accra, Ghana

HIGHLIGHTS

- Fossil gas leaks dominate Greater Accra's methane budget with 34% mean contribution.
- Dual $\delta^{13}C$-CH_4 and $\delta^{2}H$-CH_4 isotopes distinguish biogenic from fossil methane sources.
- Hierarchical Bayesian model transparently quantifies source attribution uncertainty.
- Landfills and gas infrastructure emerge as priority methane mitigation targets.
- Mobile CRDS mapping across 26 localities reveals spatial methane heterogeneity.

GRAPHICAL ABSTRACT

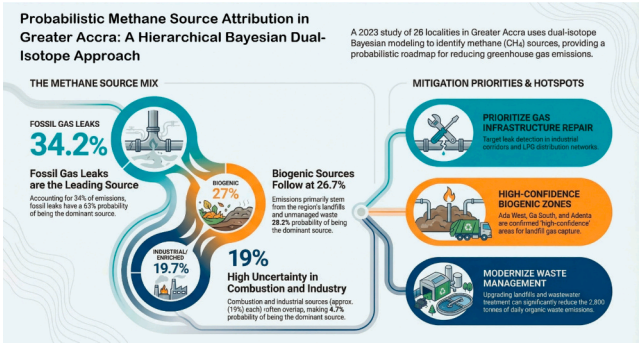

ARTICLE INFO

Keywords:
Logistic-normal priors
Posterior predictive checks
Uncertainty-aware mixing model
Keeling plot analysis

ABSTRACT

Methane is a potent greenhouse gas requiring accurate source apportionment to inform targeted mitigation, particularly in rapidly urbanizing regions where emissions arise from multiple overlapping sectors. This study aimed to quantify the methane source mix in Greater Accra, Ghana, using a hierarchical Bayesian mixing model constrained by methane mole fractions and dual stable isotope signatures ($\delta^{13}C$-CH_4 and $\delta^{2}H$-CH_4). Atmospheric methane was characterised using mobile cavity ring-down spectroscopy across 26 localities during March 2023, with observations apportioned among four aggregated source classes: Biogenic, Fossil Gas Leaks, Combustion/Transport, and Industrial/Enriched. Results were reported as posterior distributions to transparently represent attribution uncertainty. The posterior indicated Fossil Gas Leaks as the dominant contributor, with a mean contribution of 34.2% (95% HDI: 10.5–56.6%) and a 62.9% probability of being the maximal source, followed by Biogenic sources at 26.7% (95% HDI: 11.7–43.5%). Combustion/Transport and Industrial/Enriched showed substantial posterior overlap, reflecting weak separability between these anthropogenic categories. Locality-level classifications revealed high-confidence biogenic attribution at documented landfill sites (Ada West, Adenta, Ga South), while mixed-source localities exhibited lower posterior confidence. Cross-validation with Keeling-derived attributions yielded 62% agreement, with strongest consistency for Biogenic and Fossil Gas Leaks categories. This study demonstrates that dual-isotope Bayesian source apportionment can provide actionable, uncertainty-aware guidance for methane mitigation prioritization in data-limited urban environments,

* Corresponding author.
E-mail address: aquisman1989@gmail.com (E.A. Asare).

https://doi.org/10.1016/j.scitotenv.2026.181849
Received 28 January 2026; Received in revised form 28 April 2026; Accepted 29 April 2026
Available online 6 May 2026

identifying fossil fuel infrastructure leakage and solid waste management as primary intervention targets in Greater Accra's rapidly expanding urban landscape.

1. Introduction

Methane (CH_4) is a potent greenhouse gas with both natural and anthropogenic sources and reducing methane emissions is widely recognised as an important near-term climate mitigation opportunity. Accurate source apportionment is therefore needed to target mitigation efforts effectively, particularly in fast-growing urban regions where emissions can arise from multiple overlapping sectors (Menoud et al., 2022). Methane source attribution is commonly approached using bottom-up inventories and top-down atmospheric methods (Brownlow et al., 2017). Bottom-up inventories rely on activity data and emission factors, but their accuracy can be limited by incomplete local information and strong dependence of emission factors on site conditions (Cheewaphongphan et al., 2019). They can also miss episodic events that contribute disproportionately to total emissions (van der Gon et al., 2011). Top-down methods infer emissions from atmospheric measurements (Elguindi et al., 2020), but separating total enhancements into source-specific contributions remains difficult because urban plumes often mix rapidly and different sources can co-occur.

Stable isotope measurements provide an additional constraint because methane from different processes can carry distinct isotopic compositions. Carbon isotopes ($\delta^{13}C$-CH_4) are useful for broad separation between relatively depleted microbial methane and less depleted thermogenic or combustion-related methane, but source classes can still overlap substantially in $\delta^{13}C$ space (Zazzeri et al., 2017; Menoud et al., 2021). Hydrogen isotopes ($\delta^{2}H$-CH_4) provide an additional, orthogonal constraint because source categories that are difficult to separate using $\delta^{13}C$ alone can occupy different positions in dual-isotope space (Townsend-Small et al., 2015; Menoud et al., 2021; Fiehn et al., 2023). For this reason, dual-isotope constraints are increasingly valued, especially in regions where $\delta^{13}C$ alone cannot reliably separate thermogenic and microbial sources (Menoud et al., 2021; Fiehn et al., 2023). In this study, $\delta^{2}H$-CH_4 was therefore used not as a redundant measurement, but as a complementary discriminator, because overlap still remains for some anthropogenic categories (Ramsden et al., 2022; Meyer et al., 2022). Here, $\delta^{2}H$-CH_4 served two specific roles in source attribution. First, it provided a second isotopic axis that complements $\delta^{13}C$-CH_4 and improves separation where carbon-isotope domains overlap. Second, when analysed jointly with $\delta^{13}C$-CH_4 in the Bayesian framework, it reduced the risk of over-assigning mixed plumes to a single source class, because posterior source fractions were only strongly constrained where both isotope systems were mutually consistent with the same source mixture. $\delta^{2}H$-CH_4 was therefore treated as a complementary constraint that improves identifiability rather than as a redundant duplicate of $\delta^{13}C$-CH_4.

Previous mobile methane-isotope studies demonstrate that isotope-enabled source attribution is well established but also show that its performance depends strongly on regional source mixtures and source-signature overlap. For example, Maher et al. (2014) mapped CH_4 and CO_2 concentrations and $\delta^{13}C$ values in Australian coal seam gas fields using mobile CRDS, reporting methane enhancements up to 6.89 ppm and showing that mobile isotope measurements can support qualitative source assessment in large gas-field settings. Lu et al. (2021) later extended this approach in the Surat Basin, Queensland, by measuring both $\delta^{13}C$–CH_4 and δD–CH_4 from plume samples and deriving source signatures using Keeling plots; they concluded that dual-isotope information improves discrimination among coal seam gas, agricultural, wastewater, and other sources where methane mole fraction alone is insufficient. These studies provide important methodological context for the present work: the novelty here is not the measurement of methane isotopes per se, but the application of a hierarchical Bayesian dual-isotope mixing framework to a rapidly urbanizing West African city where fossil fuel, waste, wetland, transport, and industrial sources overlap within a compact urban domain.

Greater Accra, Ghana, a rapidly urbanizing West African city, provides a relevant case study because multiple methane-producing activities coexist within a compact and rapidly urbanizing region. The region has been identified as a major contributor to Ghana's methane emissions from solid waste disposal, accounting for 57% of the national total in 2019 (Environmental Protection Agency (EPA), 2022). Over the same period, methane emissions from solid waste disposal increased substantially at the national scale, consistent with rising waste generation and pressure on disposal infrastructure (Environmental Protection Agency (EPA), 2022). At the same time, Greater Accra contains additional plausible methane source environments, including wetlands and wastewater systems, dense transport corridors with combustion emissions, industrial zones, and fuel distribution activities supported by extensive LPG use and a limited natural-gas pipeline footprint concentrated in industrial areas (Asare et al., 2025). Against this background, the study objective was to quantify the methane source mix in Greater Accra using observations and a hierarchical Bayesian mixing model constrained by methane mole fraction and dual isotopes. Specifically, this study addressed three questions. First, what source mixture was most consistent with the observed CH_4, $\delta^{13}C$–CH_4, and $\delta^{2}H$–CH_4 patterns across the 26 surveyed localities? Second, did the dual-isotope constraint provide sufficient information to separate broad source classes in a complex urban environment, and where did posterior uncertainty remain large? Third, could locality-level posterior probabilities support practical prioritization by identifying locations with relatively high-confidence attribution versus locations that remained mixed or weakly identifiable? To answer these questions, we characterised atmospheric methane using mobile cavity ring-down spectroscopy across Greater Accra during March 20–25, 2023, and then applied a hierarchical Bayesian mixing model to apportion observations among four aggregated source classes (Biogenic; Fossil Gas Leaks; Combustion/Transport; Industrial/Enriched). Results were reported as posterior distributions and locality-level posterior probabilities to support transparent interpretation of both inferred source ranking and attribution uncertainty. By extending dual-isotope, uncertainty-aware source apportionment to Greater Accra, this work aimed to provide evidence that can inform methane mitigation priorities in a rapidly urbanizing West African context.

2. Methodology

2.1. Study area

The Greater Accra region (Fig. 1) is the country's most urbanized, with a population of more than five million. It is ethnically diverse, with sizeable Ga-Dangme and Akan communities, and is anchored by Accra, the national capital where colonial-era buildings, bustling traditional markets, and contemporary high-rises coexist. As Ghana's main administrative, economic, and educational hub, the metropolis concentrates government institutions, multinational firms, and leading universities. Rapid outward growth has also produced a network of satellite towns and expanding suburbs, each facing distinct development pressures.

Energy supply in the region reflects a mixed distribution system. Roughly 60% of households meet domestic cooking needs using liquefied petroleum gas (LPG) cylinders, whereas natural-gas pipelines are largely confined to industrial enclaves and a limited number of commercial districts. This uneven expansion of the gas network shapes both access to modern energy and the spatial pattern of potential methane emissions. Mobility and commerce are supported by key transport corridors, especially the George Bush Highway and the Accra–Tema Motorway, which serve as major routes for movement and trade.

At the same time, the pace of urbanisation has intensified environmental and public-health challenges. Waste generation has grown faster than the capacity to collect, treat, and dispose of refuse, encouraging illegal dumping and frequent landfill overflows that elevate pollution and health risks. Reliable water supply and sanitation remain inadequate in many neighbourhoods particularly informal settlements contributing to persistent exposure to water-related illnesses and underscoring the need for stronger water and sanitation infrastructure. Air quality has also worsened with rising traffic volumes, industrial activity, and increasing reliance on charcoal; charcoal production and use, including the burning of plastics, emit substantial trace gases and particulate matter (Ministry of Environment Science Technology and Innovation (MESTI), 2021). Climate and land-use-related hazards further compound these pressures. Seasonal flooding amplified by insufficient drainage and building in flood-prone zones threatens lives, damages property, and can trigger disease outbreaks and economic disruption. Along the coast, erosion is undermining community livelihoods and weakening coastal infrastructure, driven by the combined influence of sea-level rise and human modification of shoreline systems, highlighting the urgency of mitigation and adaptation measures. In terms of waste disposal infrastructure, the region operates two engineered landfills alongside at least twelve unmanaged dumping sites. The engineered facilities collectively handle about 2800 t of municipal solid waste per day, with typical waste thicknesses of approximately 15–20 m and a composition dominated by organics (around 60%) (Bockarie et al., 2020). Leachate control is only partially implemented at the engineered sites, and methane recovery systems are not installed at any of the disposal locations.

2.2. Data collection

2.2.1. Isotopic analysis

Atmospheric methane was characterised using dual stable isotope ratios ($\delta^{13}C$–CH_4 and $\delta^{2}H$–CH_4) alongside methane mole fraction (CH_4, ppm), enabling subsequent source apportionment with isotope-informed mixing models. Stable isotope composition was reported using conventional δ-notation (‰), expressing the relative deviation of the sample isotope ratio from an internationally defined reference scale:

$$\delta = \left(\frac{R_{\text{sample}}}{R_{\text{standard}}} - 1\right) \times 1000‰ \quad (1)$$

where (R) is the heavy-to-light isotope ratio ($^{13}C/^{12}C$ for carbon; $^{2}H/^{1}H$ for hydrogen). Carbon isotopes were referenced to Vienna Pee Dee Belemnite (VPDB) and hydrogen isotopes to Vienna Standard Mean Ocean Water (VSMOW). Unless stated otherwise, uncertainty terms are reported as standard errors of the mean (SE), consistent with their later use as observation-level error inputs in the Bayesian likelihood formulation.

Continuous, high-frequency measurements of CH_4 and isotopic composition were acquired using a cavity ring-down spectroscopy (CRDS) isotopic analyser (Picarro G2201-i) mounted on a mobile platform. CRDS provides simultaneous mole fraction and isotope ratio measurements by quantifying wavelength-specific absorption of methane isotopologues under controlled cavity conditions, making it well suited for plume-resolved urban surveys. A multi-level calibration strategy was implemented to ensure traceability and comparability across the campaign. The G2201-i is a field-deployable analyser for carbon-isotope measurements in methane and carbon dioxide and was used here specifically for real-time CH_4 mole-fraction and $\delta^{13}C$-CH_4 measurements during road-based plume screening. The analyser was operated in continuous mode with CH_4 and $\delta^{13}C$-CH_4 updates every few

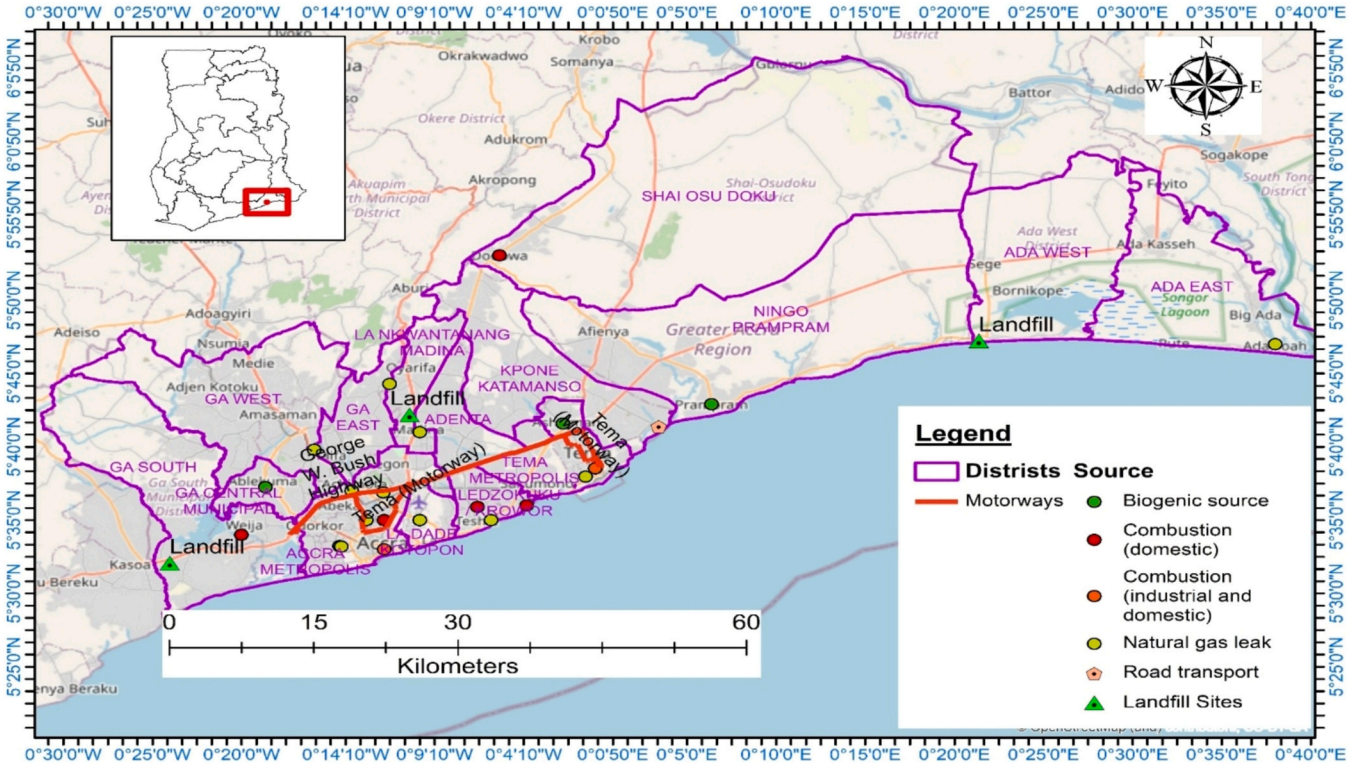

Fig. 1. Map of Greater Accra Region showing various methane sources after Asare et al. (2025).

seconds during mobile transects; under field conditions, measurement performance was approximately ±0.05 ppm for CH_4 and ~ ±0.3 ‰ for $\delta^{13}C$-CH_4. Detailed CRDS operating characteristics, including sample flow, response time, calibration, traceability, and QA/QC procedures, are provided in Appendix A. Concentration calibration was anchored to certified reference standards traceable to the WMO/NOAA CH_4 scale, spanning the concentration range encountered during mobile sampling; working standards were normalised via bracketing to confirm linearity across the calibrated domain (reported linearity $R^2 > 0.999$) (Asare et al., 2025). For $\delta^{13}C$–CH_4, primary reference materials traceable to VPDB were used to define the isotopic scale, with working standards normalised using a multi-point procedure to minimise scale compression and bias. Routine performance checks included (i) baseline stability tests using ultra-high purity zero air, (ii) periodic re-analysis of a check standard at regular intervals during field operation, and (iii) drift correction when deviations from certified isotopic values exceeded a defined tolerance. The resulting measurement performance achieved uncertainties on the order of ±0.05 ppm (expanded, k = 2) for CH_4 and ~ ±0.3 ‰ (1σ) for $\delta^{13}C$–CH_4 under field conditions, providing an empirically defensible basis for uncertainty propagation in later modelling (Asare et al., 2025).

Hydrogen-isotope measurements of methane (δ^2H-CH_4) were not obtained directly from the CRDS analyser. Instead, δ^2H-CH_4 was determined from discrete whole-air samples collected during the mobile survey from selected methane-enhanced plumes and locality-specific high-CH_4 intervals. Discrete methane-enhanced whole-air samples collected during the field campaign in Ghana were sealed in gas-tight canisters and transported under gas-tight conditions by air to the Greenhouse Gas Laboratory, Department of Earth Sciences, Royal Holloway, University of London, Egham, United Kingdom, where methane was purified from the air matrix and analysed for isotopic composition by continuous-flow IRMS. In the laboratory, methane was preconcentrated from the collected air, chromatographically separated from bulk air constituents and potential interferents, and analysed by gas chromatography coupled to pyrolysis/combustion isotope-ratio mass spectrometry (continuous-flow IRMS configuration). In this workflow, methane assigned for hydrogen-isotope analysis was quantitatively converted to H_2 by high-temperature pyrolysis prior to IRMS measurement, while carbon-isotope confirmation, where required, was obtained through combustion to CO_2. This laboratory route follows established atmospheric methane isotope methods developed for low-concentration air samples and provides a defensible pathway for δ^2H-CH_4 determination at atmospheric or plume-enhanced methane concentrations.

To maximise isotopic robustness, discrete samples targeted intervals exhibiting sustained CH_4 enhancement above background, thereby ensuring adequate methane mass for post-field δ^2H-CH_4 analysis. Larger sample volumes were used where methane enhancements were weak, while smaller containers were sufficient for stronger plumes. All accepted isotope results were linked back to their corresponding field locality, plume context, and uncertainty estimates. The final compiled dataset therefore consisted of time-stamped CH_4 mole fractions and CRDS-derived $\delta^{13}C$-CH_4 values, paired where available with laboratory-derived δ^2H-CH_4 values from matched field samples, and aggregated into analysis units suitable for isotope-informed Bayesian source apportionment.

2.2.2. Mobile detection techniques

Mobile measurements were conducted across Greater Accra during a dedicated campaign (March 20–25, 2023), covering 26 localities distributed across major administrative and emission-relevant zones (including Accra Metropolis, Tema Metropolis, Ga districts, Adenta, and Ada areas). Locality surveys were typically conducted over multi-hour transects to capture within-district heterogeneity and to increase the probability of intersecting downwind plumes under variable meteorology. The mobile survey platform consisted of a vehicle-mounted CRDS analyser operated as a continuous flow-through system during on-road sampling. Ambient air was drawn through a roof-mounted inlet to reduce self-sampling from vehicle exhaust and to improve interception of near-road plume air. Real-time CH_4 and $\delta^{13}C$-CH_4 observations were used to identify methane enhancements during the survey, and where elevated plumes were detected the vehicle could slow, loop, or briefly stop at safe locations to improve plume characterization (Asare et al., 2025) and allow collection of discrete flask/canister samples for subsequent δ^2H-CH_4 analysis. Routes were designed to (i) intersect known or suspected source environments (landfills, industrial corridors, major roadways, LPG/natural gas infrastructure zones, wetlands), (ii) include representative "background" transects away from strong point sources, and (iii) retain flexibility for opportunistic plume investigation. Where elevated CH_4 was detected, the vehicle could adopt short stationary or low-speed sampling to improve isotopic precision and stabilise signal integration in plume cores, subject to traffic and safety constraints (Asare et al., 2025). Discrete plume samples collected for laboratory δ^2H-CH_4 determination were labelled, archived under gas-tight conditions, and matched to the corresponding field interval during post-processing. This combined workflow preserved the spatial coverage and plume-screening advantages of mobile CRDS while extending the isotopic framework beyond $\delta^{13}C$-CH_4 through later laboratory determination of δ^2H-CH_4.

High-accuracy geolocation (latitude/longitude) and vehicle dynamics (speed) were recorded continuously and time-aligned with analyser output to support later spatial mapping and locality attribution. Wind speed and wind direction were recorded during surveys (and/or derived from concurrent meteorological observations), providing essential context for interpreting plume intercepts and for subsequent use in dispersion-informed interpretation.

To control for drift and ensure stability during long transects, reference gas checks were incorporated before, during, and after sampling windows, with additional mid-run checks at regular intervals. This field protocol is critical in mobile deployments because temperature, vibration, inlet humidity, and pressure fluctuations can introduce small but systematic biases if not routinely verified (Asare et al., 2025). The final compiled dataset consisted of time-stamped CH_4 mole fractions and paired isotopic compositions ($\delta^{13}C$–CH_4 and δ^2H–CH_4), aggregated by locality into discrete analysis units with associated uncertainty estimates (SE). These uncertainty estimates were retained explicitly to enable principled error propagation into the Bayesian source apportionment framework (i.e., likelihood scale informed by measurement error rather than assumed constant variance).

Detailed operational characteristics of the mobile CRDS platform, discrete plume-sampling procedures, laboratory δ^2H-CH_4 analysis, calibration/traceability, QA/QC, response characteristics, and uncertainty treatment are provided in Appendix A. For clarity of model interpretation, a dedicated notation summary for Eqs. (5)–(19) are provided in Appendix B.

2.3. Keeling-plot source-signature extraction and locality classification

Keeling-plot analysis was used as an independent, observation-based source-classification procedure against which the Bayesian locality-level classifications were compared. For each locality, isotope-qualified observations were selected from methane-enhanced intervals identified during the mobile survey. The number of observations included in each locality-level Keeling regression ranged from 4 to 19, as reported in Table 2. Following the Keeling mixing framework, the measured methane mole fraction is expressed as the sum of background and source contributions:

$$c_m = c_{bg} + c_s \tag{2}$$

and the isotope mass balance is:

$$c_m\delta_m = c_{bg}\delta_{bg} + c_s\delta_s \tag{3}$$

where $c_m$and $\delta_m$are the measured methane mole fraction and measured $\delta^{13}C–CH_4$ value, $c_{bg}$and $\delta_{bg}$are the background methane mole fraction and background isotope value, and $c_s$and $\delta_s$are the source methane contribution and source isotope signature. Rearrangement gives:

$$\delta_m = c_{bg}\left(\delta_{bg} - \delta_s\right)\left(\frac{1}{c_m}\right) + \delta_s \quad (4)$$

Thus, for each locality, $\delta^{13}C–CH_4$ was regressed against $1/c_m$, and the regression intercept was interpreted as the locality-level source signature, δ_s. Daily background methane mole fractions were estimated from the lowest 0.01% of CH_4 mole fractions recorded on each survey day to minimise residual influence from local plumes. The inferred Keeling source signatures were then assigned to literature-supported source categories and subsequently mapped to the four aggregated Bayesian classes used in this study: Biogenic, Fossil Gas Leaks, Combustion/Transport, and Industrial/Enriched. These Keeling-derived labels were not used to force the Bayesian posterior; instead, they served as an independent comparator for assessing whether the dual-isotope Bayesian model produced locality-level classifications consistent with the simpler $\delta^{13}C$-based source-signature approach. Representative Keeling regressions are provided in Fig. 2, and the locality-level Keeling-to-Bayesian class mapping is reported in Section 3.23.

2.4. Bayesian modelling framework

2.4.1. Overview of the probabilistic model

A hierarchical Bayesian mixing model was implemented in PyMC, an open-source Python library for Bayesian statistical modelling and probabilistic programming, to apportion atmospheric methane observations to multiple source classes. The model jointly constrained source contributions using (i) measured methane mole fractions (CH_4), (ii) optional source–receptor footprint sensitivities, (iii) mobile CRDS-derived $\delta^{13}C$-CH_4 values, and (iv) laboratory-derived $\delta^{2}H$-CH_4 values obtained from discrete plume samples collected during the mobile campaign. The final dual-isotope dataset was assembled by linking post-field $\delta^{2}H$-CH_4 results to the corresponding sampled plume or locality, thereby allowing simultaneous carbon- and hydrogen-isotope constraints where paired observations were available.

2.4.2. Observation and forward model

For clarity, all symbols used in Eqs. (5)–(19) are defined at first use in the text and summarized in Appendix B. In brief, $i$indexes samples/localities, $s$indexes source classes, f_{is} denotes the latent fractional contribution of source $s$to sample i, E_s denotes source-emission scaling, H_{is} denotes source–receptor footprint sensitivity, and isotope-specific terms distinguish observed values, modelled values, source signatures, and associated uncertainty components.

2.4.2.1. Methane concentrations. Let samples be indexed by ($i \in 1,\ldots,N$) and sources by ($s \in 1,\ldots,S$). Denote the latent fractional contribution of source (s) to sample (i) by ($f_{i,s}$), the source emission scaling by (E_s), and the footprint sensitivity by ($M_{i,s}$). Where footprint data were unavailable, a uniform footprint matrix was assumed:

$$M_{i,s} = 1 \qquad \forall i, s. \quad (5)$$

The expected methane mole fraction for each sample was modelled as a background term plus the footprint-weighted source contributions:

$$\mu_{CH_4,i} = C_{\mathrm{bg}} + \sum_{s=1}^{S} f_{i,s}, M_{i,s}, E_s. \quad (6)$$

where i indexes samples, s indexes source classes, and all other symbols are defined in Appendix B, Table B1.

All observations were treated as conditionally independent given model parameters (i.e., no explicit temporal correlation was introduced).

2.4.2.2. Isotopic mixing. Source isotopic signatures were assumed constant within each source class and mixed linearly in fraction space. For isotope ($k \in \{^{13}C,^{2}H\}$), let ($\delta^{k}{*}s$) denote the source signature. The modelled isotopic composition at sample (i) was defined by mass balance:

$$\mu_{\delta^k,i} = \sum_{s=1}^{S} f_{i,s}, \delta_s^k = \boldsymbol{f}_i^{\top}\boldsymbol{\delta}^{\boldsymbol{k}}. \quad (7)$$

where, $f_{i,s}$ is fractional contribution of source class s to sample i, δ_s^k is isotopic signature of source class s for isotope system k, $\mu_{\delta^k,i}$ is the expected isotopic composition.

Using both isotopes the above structure was applied simultaneously to ($\delta^{13}C$) and ($\delta^{2}H$).

Conceptually, the Bayesian source-apportionment model estimates a probability distribution for the source-fraction vector rather than a single fixed solution. For each posterior draw, the model proposes a set of source fractions that sum to one, combines them with source-signature priors and the methane/isotope observation model, and

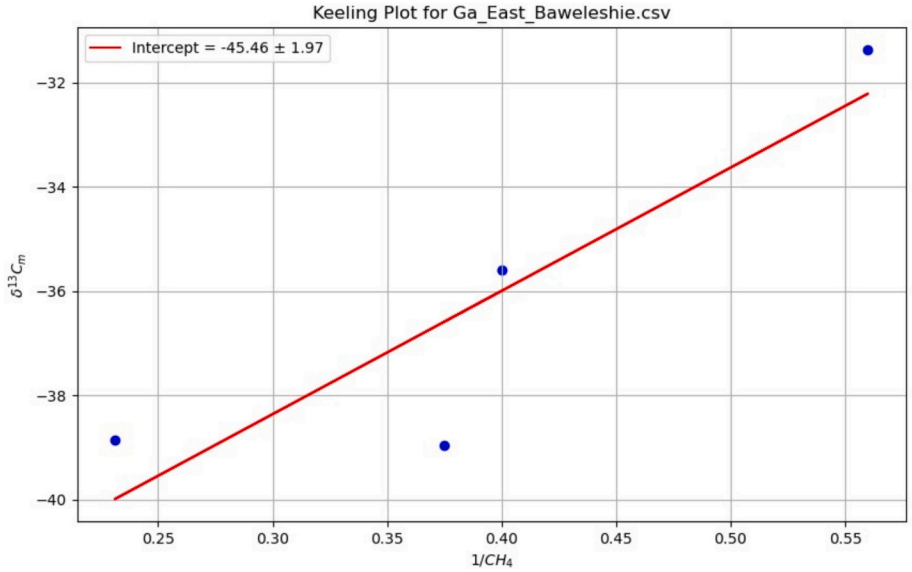

Fig. 2. Representative Keeling plot used for locality-level methane source classification. Keeling plot with y-axis in ‰ and x-axis in ppm^{-1} for Ga East.

predicts the CH_4, $\delta^{13}C$-CH_4, and δ^2H-CH_4 values expected for that mixture. Source combinations that better reproduce the observations within their uncertainty receive higher posterior support. The reported posterior means, HDIs, and 'Prob max' values therefore summarize the range of source mixtures that remain plausible given the data and prior information.

2.4.3. Priors and parameterisation

2.4.3.1. Source fractions (z and p). Fractions were represented via latent logits ($z_{i,s} \in R$) mapped to the simplex with a Softmax transform:

$$f_{i,s} = \frac{\exp(z_{i,s})}{\sum_{r=1}^{S}\exp(z_{i,r})}, \qquad \sum_{s=1}^{S} f_{i,s} = 1, f_{i,s} > 0. \tag{8}$$

A hierarchical prior anchored fractions to an inventory-derived baseline. Inventory emission scalings (E_s^{inv}) were normalised to

$$p_{0,s} = \frac{E_s^{inv}}{\sum_{r=1}^{S} E_r^{inv}}, \qquad \mu_{z0,s} = \log(p_{0,s}), \tag{9}$$

and the baseline logits were assigned:

$$z_{0,s} \sim \mathcal{N}(\mu_{z0,s}, \sigma_{inv}). \tag{10}$$

We used the diagonal logistic-normal (independent logits) covariance parameterisations for ($\boldsymbol{z_i} = (z_{i,1}, \ldots, z_{i,S})$) which is given as

$$z_{i,s} \sim \mathcal{N}(z_{0,s}, \sigma_{frac}) \quad \text{independently over } s. \tag{11}$$

This was preferred because it was much more stable and faster; often improves R-hat/ESS and good for data limited.

2.4.3.2. Source signatures and emission rates. Source isotopic signatures were assigned Normal priors informed by the inventory means and standard deviations:

$$\delta^{13}C_s \sim \mathcal{N}(\mu_s^{13C}, \sigma_s^{13C}), \qquad \delta^2H_s \sim \mathcal{N}(\mu_s^{2H}, \sigma_s^{2H}). \tag{12}$$

Emission scalingwere assigned LogNormal priors:

$$E_s \sim \text{LogNormal}(\log(E_s^{inv}), \sigma_E). \tag{13}$$

For the reduced four-source inventory, aggregated priors were formed by pooling member-source statistics using:

$$\overline{\mu} = \frac{1}{K}\sum_{j=1}^{K}\mu_j, \qquad \overline{\sigma} = \sqrt{\frac{1}{K}\sum_{j=1}^{K}\left(\sigma_j^2 + \left(\mu_j - \overline{\mu}\right)^2\right)}, \tag{14}$$

providing a conservative within- and between-member uncertainty propagation.

All sources were initialised with a common prior emission scaling ($E_s^{inv} = 10$) (unitless), since measured emission rates were unavailable.

2.4.3.3. Background terms. For the mixing model run, the methane background was assigned a Normal prior centred on a fraction of the empirical mean:

$$C_{bg} \sim \mathcal{N}(0.1, \overline{CH_4}, ; \text{sd}(CH_4)). \tag{15}$$

2.4.4. Likelihood functions and error propagation

2.4.4.1. Likelihoods. Observed methane was modelled with a Gaussian likelihood:

$$CH_{4,i}^{obs} \sim \mathcal{N}(\mu_{CH_4,i}, ; \sigma_{CH_4}). \tag{16}$$

For isotopes ($k \in \{^{13}C, ^2H\}$), observations were modelled as:

$$\delta_i^{k,obs} \sim \mathcal{N}!\left(\mu_{\delta^k,i}, ; \sigma_{tot,i}^k\right), \tag{17}$$

with ($\mu_{\delta^k,i}$) defined by the mixing model.

2.4.4.2. Uncertainty handling. When per-sample measurement standard errors (SE_i^k) were provided, likelihood scale incorporated both measurement error and an inferred residual component:

$$\sigma_{tot,i}^k = \sqrt{(SE_i^k)^2 + (\sigma_{model}^k)^2}. \tag{18}$$

Residual scale parameters were inferred with HalfNormal priors scaled to the empirical variability of each observed channel:

$$\sigma_{CH_4} \sim \text{HalfNormal}(\text{sd}(CH_4)), \quad \sigma_{model}^{13C} \sim \text{HalfNormal}(\text{sd}(\delta^{13}C)), \quad \sigma_{model}^{2H} \sim \text{HalfNormal}(\text{sd}(\delta^2H)). \tag{19}$$

2.5. Computational inference

Posterior inference was performed using PyMC's NUTS sampler. For the documented reduced four-source run, the configuration comprised four parallel chains, 2000 tuning iterations per chain, and 10,000 retained posterior draws per chain, with a target acceptance probability of 0.98 and random seed 42 (four cores). Model checking and convergence assessment were supported through standard posterior diagnostics and posterior predictive checks (e.g., trace, PPC, and energy diagnostics were produced for the run) (Abril-Pla et al., 2023).

2.6. Implementation in Python

The Bayesian source apportionment of methane emissions was implemented using Python, a high-level programming language (Python Software Foundation, 2021). This study utilized several Python libraries. PyMC, a library for Bayesian statistical modelling and probabilistic machine learning, was used to construct and fit complex Bayesian models using Markov chain Monte Carlo (MCMC) sampling (Abril-Pla et al., 2023). NumPy was employed for numerical operations, providing support for arrays and mathematical functions to operate on these arrays. For data manipulation and analysis, the Pandas library was used, offering data structures and operations for manipulating numerical tables and time series.

3. Results

3.1. Observational variability across Greater Accra

3.1.1. Survey coverage and trace dataset

The mobile methane survey of Greater Accra was conducted during March 20–25, 2023, utilizing a vehicle-mounted Picarro G2201-i cavity ring-down spectroscopy (CRDS) isotopic gas analyser (Asare et al., 2025). The measurement route encompassed 26 distinct localities distributed across the Greater Accra Region, including key areas such as Ga Central, Adenta, Tema West, Accra Metropolis, and Ada East (Table 2). Sampling was organized by locality and time period, with individual surveys typically spanning 2–4 h per site to capture spatial heterogeneity in methane concentrations and isotopic signatures under varying meteorological conditions (Asare et al., 2025). The number of samples included in Keeling plot analysis per locality ranged from 4 to 19, with most localities yielding 9–19 observations suitable for isotopic source characterization (Table 2). Although the number of isotope-qualified observations per locality is modest, the study objective was not to derive a fully resolved site-specific emissions inventory, but to perform uncertainty-aware source screening across four aggregated source classes. The hierarchical Bayesian framework therefore uses the available locality-level information to estimate probabilistic source mixtures while allowing uncertainty to widen where observations are sparse. For this reason, the results are interpreted as posterior source rankings and locality-level probabilities rather than as exact

deterministic fractions for every site.

The survey revealed substantial spatial heterogeneity in atmospheric methane concentrations across the study region. Because the source-attribution workflow focused on methane-enhanced plume intervals, Table 2 reports the maximum plume CH_4 mole fraction observed during each isotope-qualified locality survey. These maxima are useful for identifying short-lived or spatially localized emission events relevant to Keeling-plot source characterization, but they should not be interpreted as locality-average exposure concentrations. Maximum CH_4 mole fractions ranged from 1.88 ppm in Ablekuma North to 5.89 ppm in Tema Metropolis, with an overall mean enhancement of approximately 3.3 ppm across sampled localities (Table 2). Notably, two urban centres exhibited particularly pronounced elevations: Tema Metropolis attained the highest concentration at 5.89 ppm with $\delta^{13}C = -24 \pm 2$ ‰, while Accra Metropolis recorded 5.08 ppm with $\delta^{13}C = -24 \pm 3$ ‰ (Table 2). These concentrations demonstrated right-tailed distributional behaviour characteristic of episodic point-source emissions in urban settings. Intermediate enhancements (3–4 ppm) clustered in the central and southeastern portions of Accra, including La Dade-Kotopon (4.06 ppm) and Ledzokuku (4.69 ppm), whereas peripheral northern and western localities (e.g., Ablekuma North, Ga West) exhibited lower baseline concentrations between 1.88 and 2.08 ppm. This spatial structure suggested a gradient transitioning from less urbanized peripheries toward industrial and commercial centres.

3.1.2. Dual-isotope space and qualitative source separation

The $\delta^{13}C$-CH_4 isotopic signatures spanned a wide range from -55 ± 2 ‰ to -21 ± 2 ‰, encompassing the isotopic domains of biogenic, mixed, and thermogenic methane sources (Table 2). Distinctly depleted values ($\delta^{13}C \leq -50$ ‰) were concentrated in three localities: Ada West (-55 ± 2 ‰), Adenta (-54 ± 2 ‰), and Ga South (-52 ± 3 ‰), consistent with landfill or microbial anaerobic respiration signatures (Asare et al., 2025). Intermediate depleted signatures (-49 to -45 ‰) appeared in Ashaiman, Ga Central, and Ningo Prampram, characteristic of biogenic sources including wastewater treatment and agricultural waste decomposition (Table 2). In contrast, less negative values (-24 to -27 ‰) dominated Accra Metropolis, Tema Metropolis, and Kpone Katamanso, indicating significant contributions from combustion and fossil fuel sources. Mixed signatures ranging from -40 to -44 ‰ appeared across multiple localities (e.g., Ayawaso Central, Korle Klottey, La Dade-Kotopon), suggesting complex source admixtures where biogenic and thermogenic contributions coexist (Table 2). This isotopic heterogeneity demonstrated that Greater Accra's methane budget reflects overlapping emissions from distinct source categories rather than a single dominant pathway.

Four localities exemplified distinct source typologies. Ada West presented the clearest biogenic signature (-55 ± 2 ‰, 2.03 ppm CH_4), consistent with wetlands or landfill emissions as noted in the source attribution (Table 2). Conversely, Tema Metropolis exhibited strong thermogenic character (-24 ± 2 ‰, 5.89 ppm), reflecting dominance by combustion and fossil fuel activities in an industrial zone (Table 2). Ashaiman (2.48 ppm, -49 ± 2 ‰) demonstrated a moderately depleted biogenic signature aligned with wastewater or agricultural sources (Table 2). Finally, Ayawaso Central (2.05 ppm, -44 ± 4 ‰) and Ayawaso West (3.07 ppm, -40 ± 2 ‰) displayed ambiguous mixed-source signatures, neither clearly biogenic nor thermogenic, suggesting that these localities experience contemporaneous emissions from multiple incompletely resolved source classes (Table 2). These contrasting examples illustrated why Bayesian apportionment methods were necessary to quantify fractional source contributions in this complex urban environment.

3.2. Bayesian source apportionment

3.2.1. Model output summary and reporting conventions

The hierarchical Bayesian mixing model jointly constrained methane observations using measured mole fractions (CH_4), dual isotopic compositions ($\delta^{13}C$ and $\delta^{2}H$), and optional source–receptor footprint sensitivities to estimate fractional contributions from four aggregated source classes: Biogenic, Fossil Gas Leaks, Combustion/Transport, and Industrial/Enriched. The Bayesian model estimates source fractions on the simplex, where contributions range from 0 to 1 and sum to unity, with central tendencies expressed as posterior mean ± 95% highest density interval (HDI). For readability, source contributions are reported in the text and tables as percentages, obtained by multiplying posterior fractions by 100. Figures retain the model-native fractional scale, and values can be converted to percentages by multiplying by 100. Posterior distributions were derived from 10,000 retained draws per chain across four parallel MCMC chains, with convergence assessed via Gelman–Rubin statistics ($\hat{R}$) and effective sample size metrics (Table 3). This probabilistic framework explicitly quantifies source identifiability and allows transparent reporting of parametric uncertainty, which is essential for policy-relevant source attribution in complex urban environments.

3.2.2. Posterior source contributions and uncertainty

The posterior distribution indicated Fossil Gas Leaks as the dominant source contributor, with a posterior mean contribution of 34% (95% HDI: 8–59%), followed by Biogenic sources at 28% (95% HDI: 10–46%) (Fig. 3, Table 4). These percentages correspond to model-native posterior fractions of 0.34 and 0.28, respectively. The remaining categories were smaller and strongly overlapping: Combustion/Transport contributed 19% (95% HDI: 7–32%), while Industrial/Enriched contributed 18% (95% HDI: 6–34%) (Table 4). When ranked by posterior probability of being the maximum contributor, Fossil Gas Leaks had the highest probability of dominance (62.9%), followed by Biogenic sources (28.2%) (Table 4). Combustion/Transport and Industrial/Enriched had much lower probabilities of being dominant (4.3% and 4.7%, respectively), indicating weak separability between these smaller anthropogenic source classes. This ordering suggests that Greater Accra's methane budget is substantially influenced by fossil fuel infrastructure leakage, with biogenic sources from waste and agricultural systems forming the second-largest component.

The posterior distributions exhibited substantial overlap and asymmetry, particularly between the smaller source classes (Fig. 4). Because the figure displays the model-native fractional scale, values are discussed here as percentages for readability, with percentages obtained by multiplying the plotted fractions by 100. The boxplot visualization showed that Fossil Gas Leaks had the widest interquartile range, approximately 24–51%, and the broadest whisker range, approximately 2–80%, indicating the highest posterior uncertainty despite being the dominant inferred source (Fig. 4). Biogenic sources were more tightly constrained, with a median contribution of approximately 26%, an interquartile range of 24–33%, and whiskers spanning approximately 9–48%, reflecting moderate identifiability (Fig. 4). In contrast, Combustion/Transport and Industrial/Enriched showed nearly identical and highly overlapping distributions, with median contributions of approximately 18% and 17%, respectively, and whisker ranges of approximately 2–36% and 2–42%. This overlap indicates substantial posterior trade-offs and weak separability between these anthropogenic categories (Fig. 4). Despite the wide uncertainty, the posterior supported a fossil-dominant scenario as plausible. However, the broad allocation trade-offs among fossil, combustion-related, and industrial/enriched fractions show that a range of source partitions remained consistent with the observational constraints and model structure. This limited resolvability reflects an inherent challenge in dual-isotope discrimination when source classes have overlapping or partially degenerate isotopic signatures.

3.2.3. Locality-level posterior classification and probability

At the locality scale, posterior probabilities revealed heterogeneous source-attribution patterns across Greater Accra (Table 5). High-

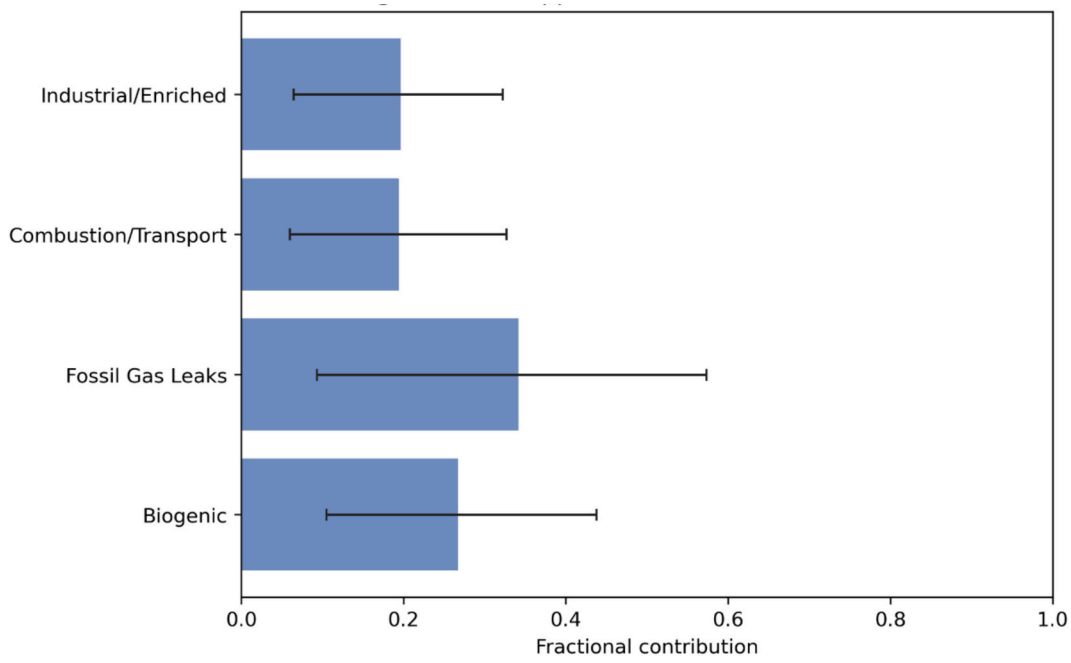

Fig. 3. Bar chart depicting the source apportionment of methane (CH_4) emissions based on $\delta^{13}C$ and $\delta^{2}H$ isotopic signatures in Greater Accra. Posterior source contributions from the Bayesian mixing model. The x-axis is shown on the model-native fractional scale; percentage contributions are obtained by multiplying values by 100.

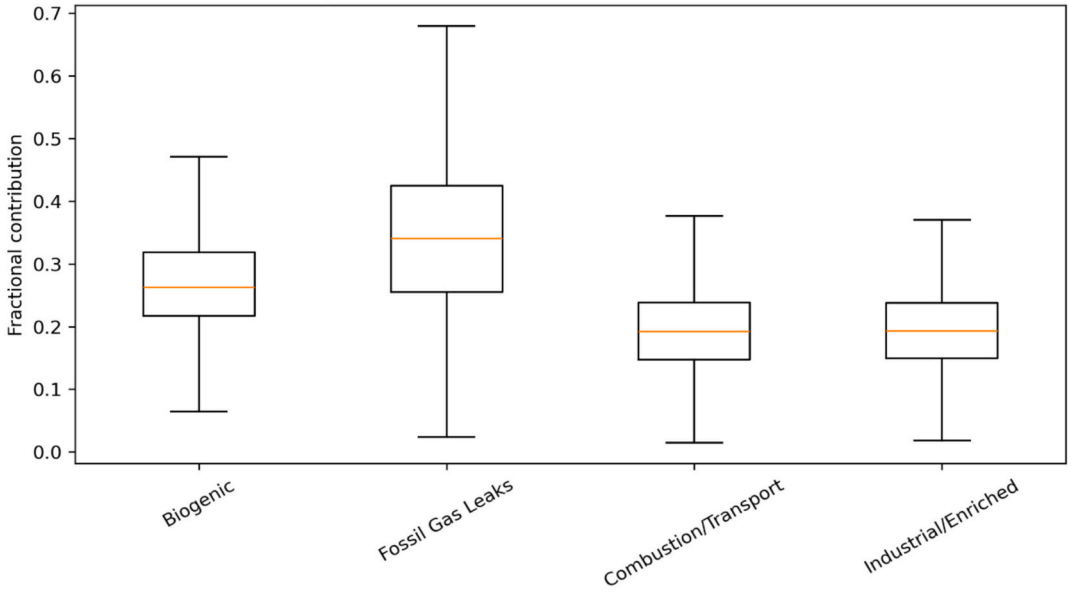

Fig. 4. Boxplot visualization of the posterior distributions of fractional contributions for methane (CH_4) emissions by source in Greater Accra based on Bayesian analysis. Contributions are displayed on the model-native fractional scale; equivalent percentages are obtained by multiplying by 100.

confidence assignments, defined as a top posterior probability of at least 50%, were mainly associated with biogenic source environments, particularly landfill- or wetland-influenced localities: Ada West (66.6% Biogenic), Adenta (56.0% Biogenic), and Ga South (58.3% Biogenic) (Table 5). In contrast, localities classified as Fossil Gas Leaks generally had lower top posterior probabilities, including Ablekuma Central (37.1% Fossil Gas Leaks), Ada East (38.7% Fossil Gas Leaks), and Okaikwei North (38.3% Fossil Gas Leaks) (Table 5). These results indicate that fossil-gas influence was frequently inferred, but with weaker locality-level certainty than the clearest biogenic sites. Several localities also displayed ambiguous assignments, with top posterior probabilities below or only slightly above 40%, including Accra Metropolis (40.7% Industrial/Enriched), Tema Metropolis (47.5% Industrial/Enriched), and Ningo Prampram (43.5% Fossil Gas Leaks) (Table 5). This pattern suggests mixed source influences and limited posterior confidence in several urban and industrial localities, consistent with overlapping isotopic signatures among anthropogenic methane sources.

3.2.4. *Agreement with keeling-based attribution*

Comparison between Bayesian posterior classifications and independent Keeling-based source assignments (Asare et al., 2025) revealed an overall match rate of 0.615 (16 of 26 localities; Table 7). The

confusion matrix indicated strongest agreement for Biogenic (3 of 6 localities) and Fossil Gas Leaks (12 of 12 localities), whereas substantial disagreement concentrated among Combustion/Transport and Industrial/Enriched classifications (Table 6). Specifically, four combustion/transport assigned localities were misclassified as Industrial/Enriched by the Bayesian model, and three additional combustion localities were assigned to Fossil Gas Leaks (Table 6), reflecting the aforementioned identifiability challenges among overlapping anthropogenic sources.

3.3. Model checking and inference diagnostics

3.3.1. Chain behaviour and parameter posteriors

Visual inspection of Markov chain Monte Carlo (MCMC) traces revealed stationary, well-overlapped behaviour across all four parallel chains, with no evidence of drift or transient phases (Fig. 5). The posterior density for the background methane term exhibited non-Gaussian, bimodal structure with a sharp mode near −2.7 and broader mass centred around −1.6, suggesting potential partial confounding between background and source contribution parameters under the observation model (Fig. 5). The inferred observational means demonstrated tight concentration relative to source fractions: $\mu_{(CH_4)}$ centred at approximately 3.1 ppm, $\mu_{(\delta^{13}C)}$ peaked near −37.5 ‰, and $\mu_{(\delta^2H)}$ near −212 ‰, all with substantially reduced posterior spread (Fig. 5). In contrast, source fraction posteriors were bounded and asymmetric by design (simplex constraints). Fossil Gas Leaks exhibited the broadest posterior support with a noticeable density peak near 0.53, whereas Biogenic displayed more stable attribution around 0.26–0.28 (Fig. 5). Industrial/Enriched showed a sharp low-fraction spike around 0.08, indicating that the posterior frequently assigned minimal industrial contribution in subsets of the parameter space, reinforcing posterior trade-offs and incomplete identifiability (Fig. 4).

3.3.2. Convergence and effective sample size

Gelman–Rubin convergence statistics ($\hat{R}$) indicated adequate chain mixing for most parameters, with all reported $\hat{R}$ values equal to 1.0 for background and observational means (Table 3). However, source fraction convergence showed mild heterogeneity: Combustion/Transport and Biogenic attained $\hat{R} = 1.001$ and 1.003, respectively, while Fossil Gas Leaks and Industrial/Enriched exhibited slightly elevated $\hat{R} = 1.004$ (Table 3), signalling incomplete mixing for dominant and less-separated fractions. Effective sample sizes (ESS) for bulk and tail were generally adequate, with ESS bulk ranging from 2206 to 3125 and ESS tail from 3661 to 6714 across fractions (Table 3). These elevated $\hat{R}$ values for fossil and industrial components, though below conventional alarm thresholds ($\hat{R} < 1.01$), warranted cautious interpretation of wide credible intervals for these source classes and suggested that posterior uncertainty bounds should be considered conservative rather than optimistic.

3.3.3. Posterior predictive checks

Posterior predictive checks across all three observables demonstrated adequate overall calibration (Fig. 6). The posterior predictive distribution for total CH_4 was unimodal with peak at 2.8–3.0 ppm and right-skewed tail extending to ~6.5 ppm, encompassing observed concentrations spanning 2–6 ppm (Fig. 6A). For $\delta^{13}C$, the predictive density centred near −38 ‰ with substantial mass from −55 to −25 ‰, broadly covering the observed range (Fig. 6B). Similarly, δ^2H predictions peaked around −210 ‰ with support approximately −320 to −100 ‰, capturing observed clustering near −200 to −210 ‰ (Fig. 6C). However, the observed histograms exhibited sharper, more discrete peaks relative to the smoother posterior predictive curves, consistent with finite sampling, measurement resolution, or unmodeled substructure. This predictive smoothness, particularly for δ^2H, suggested residual variability was absorbed by the likelihood rather than resolved as distinct source sub-modes, indicating partial identifiability among sources.

3.3.4. HMC energy and BFMI diagnostic

Energy and Bayesian fraction of missing information (BFMI) diagnostics revealed suboptimal NUTS sampler performance (Fig. 7). The energy transition distribution was noticeably narrower and more peaked than the marginal energy distribution, a classic signature of inefficient phase-space exploration. Consistently low BFMI values appeared across all four chains: 0.39, 0.33, 0.44, and 0.38 (Fig. 7), all substantially below commonly applied thresholds (optimal $\geq$0.8). These low BFMI values implied incomplete exploration of the typical set and potential slow autocorrelation or biased uncertainty quantification, particularly for parameters with strong correlations or funnelled geometry (Abril-Pla et al., 2023). Although posterior predictive checks supported adequate overall calibration, the energy diagnostic cautioned that reported credible intervals especially for fossil and industrial fractions should be interpreted conservatively and might underestimate true posterior variability unless supported by additional reparameterization or improved tuning.

4. Discussion

4.1. Interpretation of inferred methane source mix in Greater Accra

The Bayesian source apportionment indicates that Fossil Gas Leaks represent the largest inferred contribution to Greater Accra's methane budget, with a posterior mean of 34% (95% HDI: 10–57%), followed by Biogenic sources at 27% (95% HDI: 12–44%) (Table 4; Fig. 3 and Fig. 8). The Fossil Gas Leaks class, derived from pooling natural gas infrastructure leakage in the original inventory, likely encompasses emissions from the region's limited pipeline network serving industrial zones and potential fugitive releases from LPG distribution systems (Asare et al., 2025). The Biogenic fraction aggregates contributions from landfills, wastewater treatment plants, wetlands, and agricultural waste decomposition sources that align with Greater Accra's waste management challenges, where engineered landfills process approximately 2800 t/day of municipal solid waste without methane capture infrastructure (Asare et al., 2025). The posterior probability that Fossil Gas Leaks constitutes the dominant source reaches 63%, whereas Biogenic sources show a 28% probability of being maximal (Table 4), suggesting fossil-related infrastructure warrants priority attention for mitigation.

Despite the clear ranking of posterior means, substantial uncertainty persists in source allocation. The 95% HDIs for all four source classes overlap considerably (Fig. 8), with Combustion/Transport (19%; HDI: 6–32%) and Industrial/Enriched (20%; HDI: 7–32%) showing nearly identical posterior distributions (Fig. 3). This overlap reflects fundamental identifiability limitations: when isotopic signatures between source classes are similar or when multiple sources contribute simultaneously to observed signals, the model cannot unambiguously partition contributions. The boxplot visualization (Fig. 3) demonstrates that Fossil Gas Leaks exhibits the widest posterior spread (IQR: 24–51%), indicating that while this source ranks highest, a broad range of allocations remains consistent with the data. The posterior trade-offs between Combustion/Transport and Industrial/Enriched categories suggest these anthropogenic sources cannot be reliably distinguished using dual-isotope constraints alone, consistent with the known proximity of their $\delta^{13}C$ signatures in urban settings.

Locality-level posterior classifications (Table 5) reveal heterogeneous confidence across Greater Accra. Sites including Ada West, Adenta, and Ga South show robust Biogenic attribution with posterior probabilities of 67%, 56%, and 58% respectively, all correctly matching Keeling-based classifications. These localities correspond to documented landfill sites and wetland areas where strongly depleted isotopic signatures ($\delta^{13}C$: −52 to −55 ‰) provide clear discrimination (Asare et al., 2025). Conversely, sites like Ayawaso Central, Ayawaso West, and Tema West are assigned to Fossil Gas Leaks with moderate confidence (42–48%), reflecting the “fossil methane source mix” attributions from Keeling analysis. Mixed or ambiguous classifications concentrate in

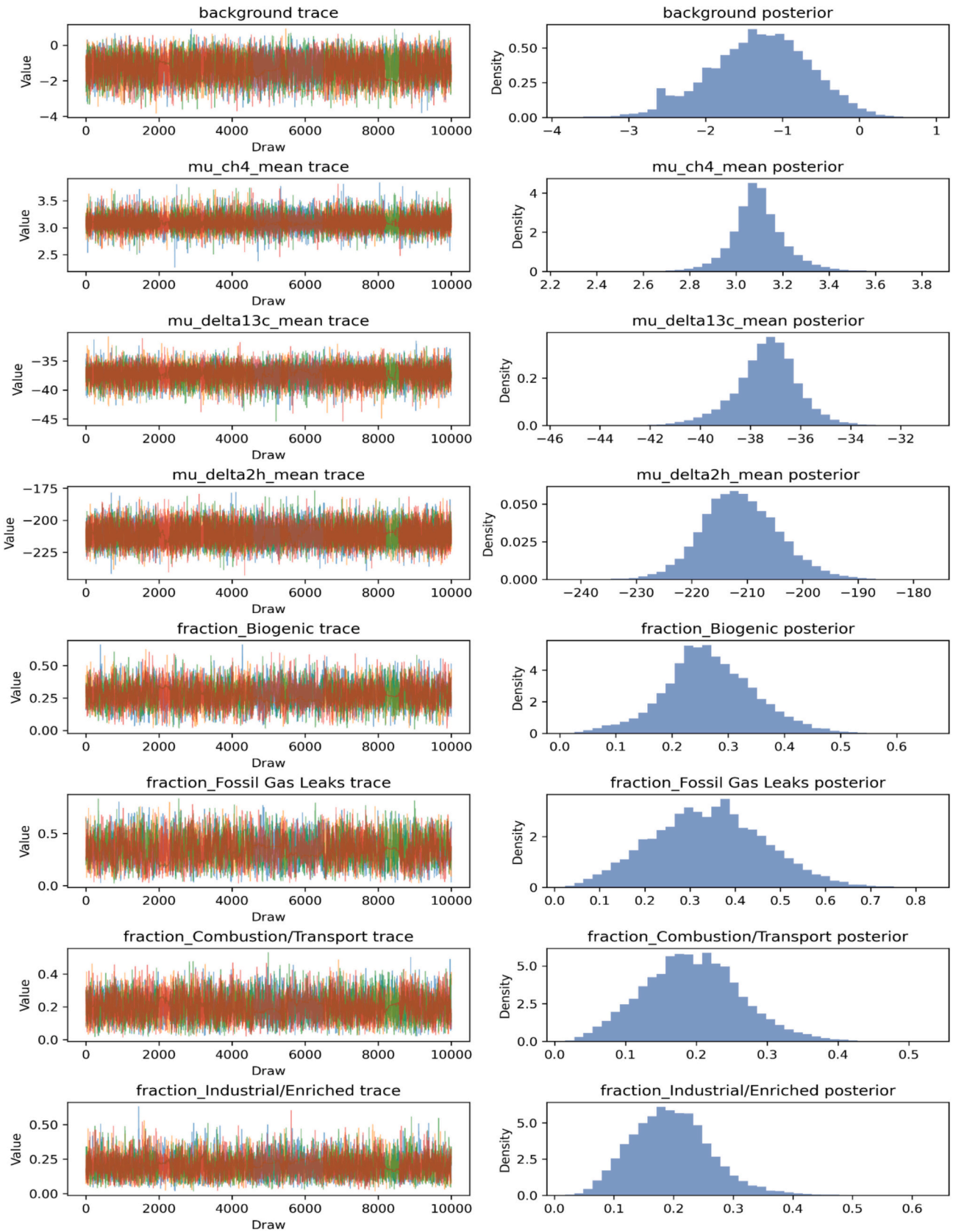

Fig. 5. Trace plots (left panels) and marginal posterior distributions (right panels) for key parameters in the Bayesian source-apportionment model. In the trace panels, the differently coloured lines, including the brown and green lines, represent independent MCMC chains and are shown to assess chain mixing and convergence; they do not represent different source categories. In the posterior panels, the blue histograms show the marginal posterior distribution for each parameter after pooling retained draws across chains. Parameters shown include the background methane term, expected observation-level means, and the fractional contributions of the four aggregated source classes.

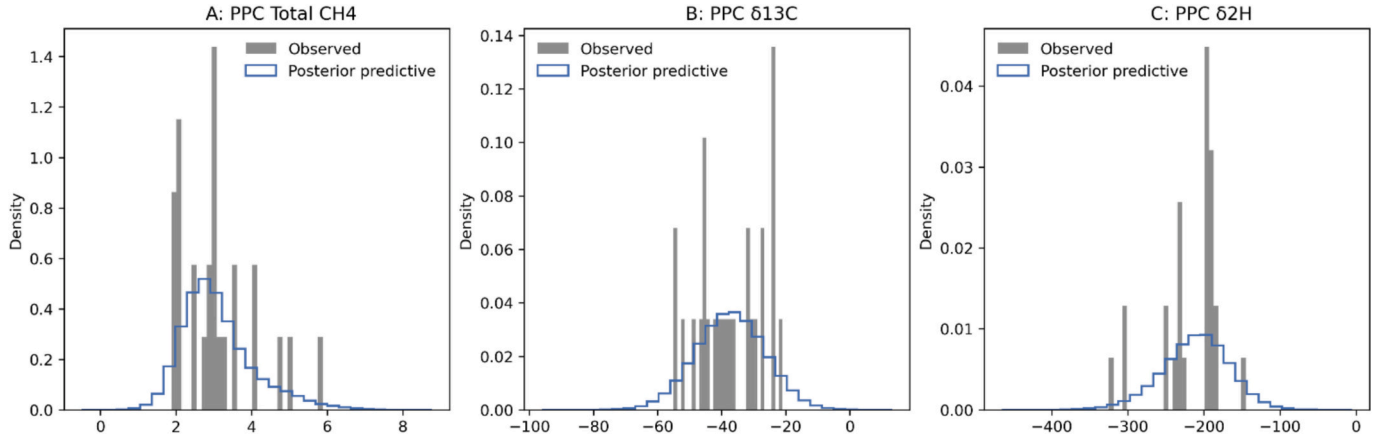

Fig. 6. Predictive checks for Bayesian Source Apportionment model of methane emissions: (A) Total methane, (B) $\delta^{13}C$ isotopic ratio, (C) $\delta^{2}H$ isotopic ratio, comparing observed data with posterior predictions in Greater Accra.

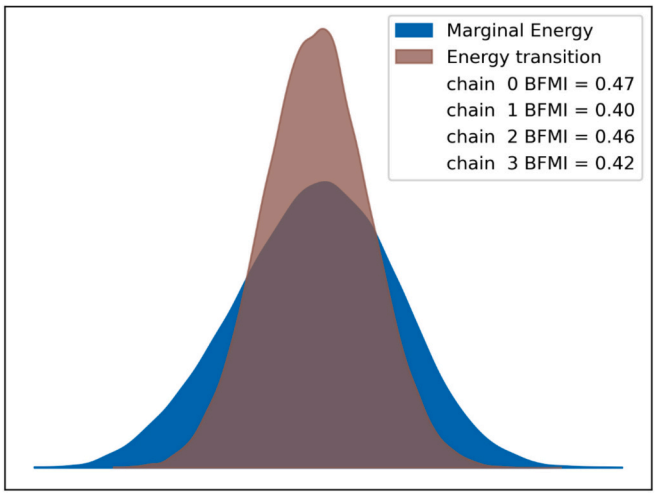

Fig. 7. Bayesian Model Convergence Diagnostic plot with overlapping marginal energy and energy transition distributions for two MCMC chains, both exhibiting a BFMI of 0.97.

areas where Combustion/Transport competes with Industrial/Enriched notably Accra Metropolis, Ledzokuku, and Tema Metropolis where isotopic signatures fall within overlapping ranges and posterior top-probabilities remain below 50%.

The Greater Accra isotope range is consistent with the broad source domains reported in previous urban and mixed-source studies, but the local source mixture differs in important ways. Strongly depleted $\delta^{13}C$–CH_4 values at Ada West, Adenta, and Ga South are consistent with microbial methane from wetlands, landfill, or waste-related anaerobic decomposition, whereas enriched values in Accra Metropolis, Tema Metropolis, Ledzokuku, and Kpone Katamanso fall closer to combustion, industrial, or fossil-associated domains. Comparable Australian coal seam gas studies show that mobile isotope mapping can identify source-relevant plumes, but also that source attribution becomes difficult where multiple sources coexist or where $\delta^{13}C$ domains overlap (Lu et al., 2021). The present Bayesian framework addresses this problem by reporting posterior source probabilities and uncertainty intervals rather than assigning deterministic source labels from isotope values alone.

4.2. Methodological insights and cross-validation with Keeling attribution

The simultaneous constraint from $\delta^{13}C$ and $\delta^{2}H$ provides enhanced source separation compared to single-isotope approaches, particularly for distinguishing biogenic sources (landfills, wetlands) from fossil gas leaks, which occupy different positions in dual-isotope space (Table 1). However, even with both isotopes, certain source pairs remain poorly separable specifically, combustion and industrial processes share overlapping isotopic domains, while within-class variability for sources like "fossil methane source mix" spans ranges that confound attribution. The hierarchical Bayesian framework quantifies this residual ambiguity through posterior distributions rather than forcing deterministic assignments.

Cross-validation with Keeling-derived attributions yields an overall match rate of 0.62 (Table 7), with 16 of 26 localities showing agreement. The confusion matrix (Table 6) reveals that mismatches cluster predominantly among Combustion/Transport classifications: of eight sites assigned to this category by Keeling analysis, only one matches the Bayesian top-source assignment. This discordance reflects mixture complexity at urban sites where combustion, transport, and industrial sources co-occur, alongside within-class isotopic variability documented across global studies (Menoud et al., 2021; Zazzeri et al., 2017). The Biogenic and Fossil Gas Leaks categories show stronger cross-method consistency, supporting their robustness as distinguishable source classes.

Posterior predictive checks (Fig. 6) demonstrate that the model reproduces observed distributions for CH_4, $\delta^{13}C$, and $\delta^{2}H$, with posterior predictive densities covering the empirical support and capturing central tendencies. However, observed data exhibit sharper peaks than predictive distributions, suggesting residual heterogeneity not captured by the four-class aggregation. Convergence diagnostics indicate adequate chain mixing: R-hat values of 1.00 across all fraction parameters and effective sample sizes exceeding 2200 (Table 3) support reliable posterior inference. Nevertheless, energy diagnostics (Fig. 7) reveal BFMI values of 0.33–0.44, below recommended thresholds, indicating that posterior geometry presents sampling challenges. Consequently, conclusions regarding the precise magnitude of source contributions particularly for overlapping categories should be interpreted with appropriate caution, while the qualitative ranking remains defensible.

4.3. Implications for mitigation and monitoring in Greater Accra

The posterior source apportionment provides actionable guidance for methane mitigation prioritization in Greater Accra. Fossil Gas Leaks emerges as the dominant contributor with a posterior mean of 34% and the highest probability of being the maximal source (63%; Table 4), indicating that pipeline and infrastructure leak detection and repair programs warrant primary attention. Given that natural gas pipeline infrastructure in Greater Accra remains predominantly restricted to industrial zones and select commercial areas, while approximately 60% of

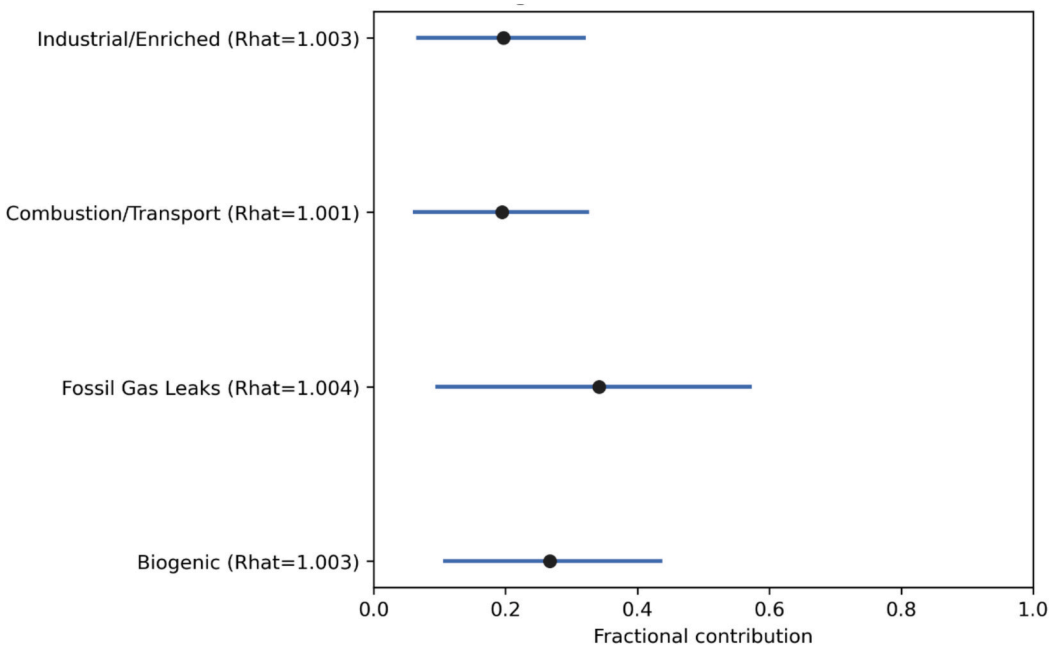

Fig. 8. Forest plot of the 95% Highest Density Interval (HDI) for fractional contributions of various methane emission sources in Greater Accra. The x-axis shows model-native posterior fractions on the simplex; multiply by 100 to obtain percentage contribution.

Table 1
Global methane isotopic signatures ($\delta^{13}C$, $\delta^{2}H$) for various sources.

Source Type	$\delta^{13}C$-CH_4 (‰, VPDB)	$\delta^{2}H$-CH_4 (‰, VSMOW)	Region / Study Context	Reference
Biogas plants	−54.6 ± 5.6	−314 ± 23	UK, NL, Turkey	(Bakkaloglu et al., 2022)
Landfills	−56.8 ± 2.3	−268 ± 2	UK	(Bakkaloglu et al., 2022)
Sewage treatment plants	−51.6 ± 2.2	−304 ± 22	UK	(Bakkaloglu et al., 2022)
Composting facilities	−54.7 ± 3.9	–	UK	(Bakkaloglu et al., 2022)
Coal mine methane (Upper Silesian Basin)	−60 to −42	−200 to −160	Poland	(Fiehn et al., 2023)
Urban/natural gas leaks	−59 to −37	−291 to −137	Krakow, Poland	(Menoud et al., 2021)
Wetlands (Arctic)	~ − 70 ± 2	–	Russia/Barents Sea	(France et al., 2016)
Freshwater (global)	−56.4 ± 1.4	−277 ± 8	Global synthesis	(Douglas et al., 2020)
Vehicle exhaust	−22 to −11	−170 to −120	USA	(Sun et al., 2025)
Abiogenic seeps (Italy)	−18	−120	Tuscan Archipelago	(Meister et al., 2018)
Oil and gas (China)	−25.7	–	Southwestern China	(Chen et al., 2025)
Sea ice (Barrow–Antarctica)	−68.5 to −13	−313 to −104	Arctic/Antarctic	(Jacques et al., 2021)
Urban air (Moscow)	−67 to −58	–	Russia	(Berezina et al., 2023)

households rely on liquefied petroleum gas cylinders for domestic fuel needs (Asare et al., 2025), targeted surveys of industrial gas distribution networks and LPG storage facilities represent logical intervention priorities. The Biogenic fraction, ranking second with a posterior mean of 0.27 and probability of 28% of being maximal (Table 4), implicates landfill and wastewater management as substantial co-contributors. The region's solid waste management infrastructure comprising two engineered landfills and at least twelve unmanaged disposal sites processing approximately 2800 t/day with 60% organic matter content and no methane capture infrastructure (Asare et al., 2025) presents clear opportunities for emissions reductions through improved landfill gas collection, waste diversion, and wastewater treatment upgrades.

Locality-level posterior probabilities (Table 5) enable differentiation between high-confidence intervention zones and areas requiring additional characterization before resource allocation. Sites where Biogenic sources dominate with strong posterior confidence Ada West (67%), Ga South (58%), and Adenta (56%) correspond to documented landfill locations and represent "high-confidence intervention zones" where landfill gas capture or waste management improvements can proceed without further attribution uncertainty. Similarly, localities assigned to Fossil Gas Leaks with moderate-to-high confidence including Ayawaso Central (48%), Ga East (45%), and Tema West (45%) merit prioritized leak detection surveys in industrial corridors. Conversely, sites exhibiting lower top-source probabilities, such as Krowor (27%), Shai Osudoku (28%), and Ablekuma North (30%), fall into "needs more data" zones where the posterior does not confidently distinguish among source categories. These mixed-attribution localities require supplementary measurements potentially including additional isotopic tracers or higher-density spatial sampling before intervention strategies can be efficiently designed. To facilitate spatial interpretation, locality-level posterior summaries are displayed on a study-area map. Fig. 9 presents the dominant posterior source class and corresponding top posterior probability at each surveyed locality centroid, complementing the tabulated probabilities in Table 5.

4.4. Strengths, limitations, and future work

The present study offers several methodological advances for urban methane source apportionment. The dual-isotope constraint, simultaneously utilizing $\delta^{13}C$ and $\delta^{2}H$ signatures, provides enhanced discrimination among source categories compared to single-isotope approaches, particularly for separating biogenic sources from fossil gas leaks occupying distinct positions in isotopic space (Table 1). The hierarchical Bayesian framework delivers probabilistic uncertainty quantification

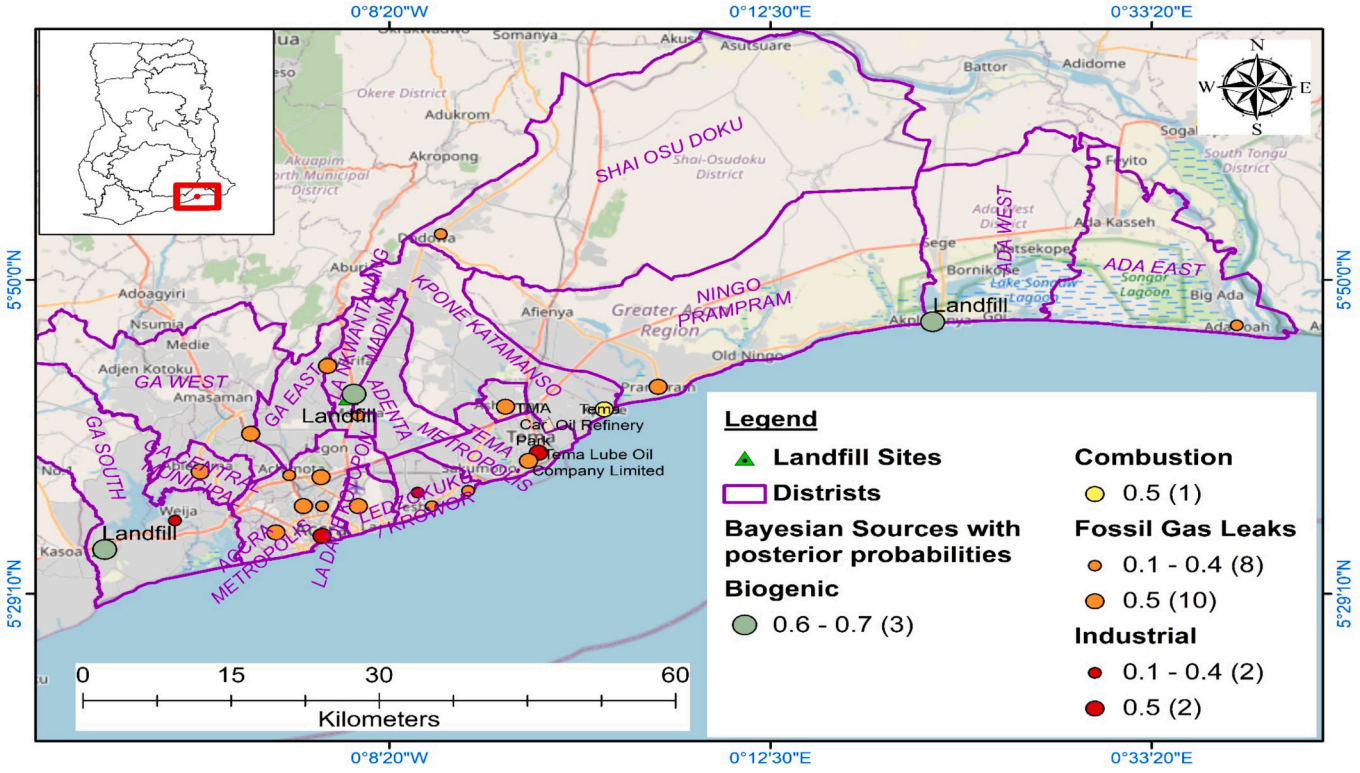

Fig. 9. Locality-centroid map of posterior methane source attribution across Greater Accra. Symbols show the dominant posterior source class at each surveyed locality, and symbol intensity/size indicates the corresponding top posterior probability showing model-native posterior fractions on the simplex; multiplying by 100 to gives percentage contribution.

through posterior distributions and highest density intervals (Table 3; Fig. 7), moving beyond deterministic point estimates to characterize the full range of plausible source allocations. Furthermore, the locality-level probabilistic classification (Table 5) enables spatially explicit mitigation planning by assigning site-specific source probabilities rather than assuming homogeneous regional contributions.

Several limitations constrain interpretation of the results. The aggregation of the original ten-source inventory into four classes Biogenic, Fossil Gas Leaks, Combustion/Transport, and Industrial/Enriched prevents finer discrimination within categories; notably, landfill emissions cannot be separated from wetland contributions within the Biogenic class, nor can enteric fermentation be distinguished from agricultural waste decomposition. The uniform footprint assumption (Eq. 5), adopted due to unavailable source-receptor sensitivity data, represents a simplification that may introduce allocation biases under heterogeneous meteorological conditions. Within-source isotopic variability contributes additional uncertainty, as evidenced by the posterior predictive checks (Fig. 6) where observed data exhibit sharper, more discrete peaks than the smoother predictive distributions, consistent with mixture heterogeneity not fully captured by the four-class structure. The energy diagnostics (Fig. 7) reveal BFMI values of 33–44% across chains, falling below commonly recommended thresholds of approximately 0.8 for robust sampling performance. These low BFMI values indicate that the sampler does not fully traverse the typical set, potentially yielding slow exploration and high autocorrelation in some parameters. While R-hat values remain acceptable at 1.00 and effective sample sizes exceed 2200 (Table 3), the energy diagnostic flags suggest that reported uncertainty bounds particularly for parameters associated with strong correlations or weak identifiability should be interpreted with added caution.

A further limitation is the modest number of isotope-qualified observations in some localities (as low as $n = 4$; Table 2), which likely contributes to weak separability and broad posterior overlap for some source classes. The present results should therefore be interpreted as uncertainty-aware source screening rather than a fully resolved emissions inventory.

The survey represents a short campaign conducted during March 20–25, 2023; therefore, the posterior source mix should be interpreted as a campaign-period attribution rather than a seasonal or annual methane budget. Temporal variability in waste decomposition, wetland emissions, traffic intensity, industrial activity, atmospheric mixing depth, rainfall, and wind conditions could shift both methane mole fractions and isotope signatures outside the campaign window. Consequently, the present results provide a probabilistic source-screening baseline for Greater Accra, while repeated wet-season/dry-season and diurnal sampling would be required to quantify temporal stability in the inferred source ranking.

Several research directions can address current limitations. Future work should prioritize additional source-specific tracers, especially ethane and propane, because these compounds are more directly diagnostic of fossil gas leakage than methane isotopes alone where source signatures overlap. CO_2 should not be treated as a simple co-emitted methane tracer in Greater Accra because urban CO_2 has multiple biogenic, traffic, biomass-burning, and industrial sources. Instead, CO_2 mole fractions and $\delta^{13}C$–CO_2, where available, should be interpreted only as contextual information alongside CH_4 mole fractions, $\delta^{13}C$–CH_4, $\delta^{2}H$–CH_4, wind fields, and local source activity data. Such associated-gas measurements would be especially valuable for resolving the present posterior overlap between Combustion/Transport and Industrial/Enriched categories. Coupling the mixing model with improved footprint calculations from back-trajectory dispersion modelling building on the HYSPLIT framework employed by Asare et al. (2025) could reduce allocation biases associated with the uniform footprint assumption. Expanded temporal sampling across seasons would capture variability in emission patterns driven by meteorological conditions and source activity cycles, addressing the limited temporal coverage of the current dataset. Finally, systematic sensitivity analyses testing alternative prior

Table 2
Key CH_4 traces detected in the Greater Accra region with $\delta^{13}C$ and $\delta^{2}H$ characteristic. Latitude is reported in decimal degrees north (°N). Longitude is reported in decimal degrees east (°E), with negative values indicating degrees west of Greenwich. CH_4 values are reported for plume-enhanced intervals used for isotopic source characterization.

Locality	Date	Time	Lat	Lon	Max CH_4 ppm	$\delta^{13}C$	$\delta^{13}C$ SE	$\delta^{2}H$	$\delta^{2}H$ SE	Wind Speed m/s	Wind Direction Deg	N Samples	Source Note[a]
Ablekuma Central	22nd March 2023	8:00 am- 10:00 am	5.553	−0.24	1.93	−31	2	−185	9	3.13	192	19	Natural gas leak
Ablekuma North	24th March 2023	6:00 am - 10:00 am	5.583	−0.2	1.88	−27	2	−250	8	2.64	186	19	Combustion
Accra Metropolis	22nd March 2023	11:00 am - 2:00 pm	5.55	−0.2	5.08	−24	3	−230	8	3.06	174	19	Combustion or road transport
Ada East	25th March 2023	3:05 pm - 5:10 pm	5.783	0.633	3.07	−36	2	−195	9	2.72	163	19	Natural gas leak
Ada West	25th March 2023	6:00 pm - 10:00 pm	5.787	0.356	2.03	−55	2	−325	13.7	3.14	187	9	Wetlands
Adenta	20th March 2023	6:00 am - 8:00 am	5.707	−0.171	3.05	−54	2	−305	27.4	2.94	206	4	Landfill
Ashaiman	21st March 2023	1:30 pm - 3:00 pm	5.693	−0.033	2.48	−49	2	−226.6	17	3.21	163	9	Biogenic source
Ayawaso Central	24th March 2023	12:00 pm - 2:00 pm	5.583	−0.167	2.05	−44	4	−198	9	3.93	177	19	Fossil methane source mix
Ayawaso North	23rd March 2023	11:00 am - 12:30 pm	5.583	−0.217	2.94	−37	3	−195	9	2.57	192	19	Natural gas leak
Ayawaso West	25th March 2023	1:00 pm - 1:45 pm	5.615	−0.201	3.07	−40	2	−190	9	2.95	171	19	Fossil methane source mix
Ga Central	20th March 2023	1:10 pm - 2:05 pm	5.621	−0.311	2.08	−46	4	−193.1	11.7	2.52	190	19	Biogenic source
Ga East	20th March 2023	2:50 pm - 4:00 pm	5.738	−0.195	2.82	−45	2	−198	19.6	3.02	182	4	Fossil methane source mix
Ga West	20th March 2022	4:00 pm - 6:00 pm	5.663	−0.265	1.97	−45	4	−198	9	2.11	169	19	Fossil methane source mix
Ga South	20th March 2023	12:32 am - 1:00 pm	5.535	−0.398	2.77	−52	3	−305	12.6	3.51	226	19	Landfill
Korle Klottey	22nd March 2023	2:50 pm - 4:00 pm	5.554	−0.242	3.22	−39	3	−190	9	2.77	152	19	Fossil methane source mix
Kpone Katamanso	22nd March 2023	5:00 pm - 6:00 pm	5.69	0.057	3.09	−21	2	−145	4.2	2.22	182	9	Road transport
Krowor	23rd March 2023	3:00 pm - 4:00 pm	5.6	−0.067	3.04	−27	2	−250	10.6	2.93	179	11	Combustion or road transport
La Dade-Kotopon	21st March 2023	6:05 am - 9:00 pm	5.583	−0.1	4.06	−41	4	−190	11.8	2.94	159	11	Fossil methane source mix
La-Nkwantanang-Madina	21st March 2023	10:00 am - 11:30 am	5.683	−0.167	3.01	−32	4	−188	19.6	3.61	185	4	Natural gas leak
Ledzokuku	25th March 2023	6:00 am - 8:45 am	5.598	−0.113	4.69	−24	2	−230	10.6	2.32	159	11	Combustion or road transport
Ningo Prampram	21st March 2023	5:00 pm - 9:00 pm	5.715	0.106	3.59	−45	1	−182	17	3.81	213	9	Biogenic source
Okaikwei North	23rd March 2023	5:00 pm - 7:00 pm	5.617	−0.23	2.03	−32	3	−188	9	2.07	172	19	Natural gas leak
Shai Osudoku	25th March 2023	10:00 am - 12:00 pm	5.884	−0.092	3.54	−30	2	−240	17.5	3.85	162	4	Combustion (domestic)
Tema Metropolis	20th March 2023	9:45 am - 11:00 am	5.642	−0.003	5.89	−24	2	−230	11.7	2.04	183	9	Combustion or road transport
Tema West	25th March 2023	2:00 pm - 3:00 pm	5.633	−0.012	2.53	−42	2	−195	13	3.82	165	9	Fossil methane source mix
Weija Gbawe	23rd March 2023	12:00 pm - 1:00 pm	5.567	−0.334	4.05	−24	2	−230	8	3.93	158	19	Combustion (domestic) or road transport

[a] Keeling/literature-supported source interpretation from Asare et al. (2025), not as a direct Bayesian result. [y] Peak areas corrected for driving speed estimated as the multiplication of peak area in ppm s and speed in m/s; s.m. signifies stationary measurements after Asare et al. (2025).

Table 3
Convergence diagnostics and effective sample sizes for key parameters in Bayesian methane source apportionment.

Source	Mean	HDI 3%	HDI 97%	R hat	Ess bulk	Ess tail
fractions[Biogenic]	0.267	0.117	0.435	1	2668	3661
fractions[Fossil Gas Leaks]	0.342	0.105	0.566	1	2206	3847
fractions[Combustion/ Transport]	0.194	0.062	0.32	1	3125	6666
fractions[Industrial/ Enriched]	0.197	0.07	0.316	1	3084	6714

Table 4
Probability of sources.

Source	Mean contribution (%)	3% HDI	97% HDI	Probability max (%)
Biogenic	26.7	11.7	43.5	28.2
Fossil Gas Leaks	34.2	10.5	56.6	62.9
Combustion/ Transport	19.4	6.2	32.0	4.3
Industrial/ Enriched	19.7	7.0	31.6	4.7

specifications, source aggregation schemes, and single-isotope versus dual-isotope configurations would strengthen confidence in the robustness of posterior conclusions and guide future inventory refinement efforts in Greater Accra and comparable rapidly urbanizing regions.

5. Conclusions

This study addressed three research questions concerning methane source attribution in Greater Accra. Regarding the source mixture most consistent with observed patterns, the hierarchical Bayesian model identified Fossil Gas Leaks as the dominant contributor (posterior mean 0.34, 63% probability of being maximal), followed by Biogenic sources (0.27, 28% probability of being maximal). This ranking implicates gas distribution infrastructure and solid waste systems as the primary methane emitters in the region, consistent with Greater Accra's limited natural gas pipeline network serving industrial zones and its landfills processing approximately 2800 t of waste daily without methane capture. Concerning whether dual-isotope constraints provided sufficient information for source separation, the analysis revealed both strengths and limitations. The simultaneous use of $\delta^{13}C$ and $\delta^{2}H$ effectively distinguished biogenic sources from fossil gas leaks, particularly at landfill sites where strongly depleted isotopic signatures provided clear discrimination. However, substantial posterior overlap persisted between Combustion/Transport and Industrial/Enriched categories, demonstrating that even dual-isotope approaches cannot fully resolve

Table 6
Keeling Bayesian Confusion matrix.

Keeling mapped	Biogenic	Combustion/ Transport	Fossil Gas Leaks	Industrial/ Enriched
Biogenic	3	0	3	0
Combustion/ Transport	0	1	3	4
Fossil Gas Leaks	0	0	12	0

Table 7
Summary of Keeling.

Total locations	Mapped locations	Match count	Match rate	Match rate confident	Confidence threshold
26	26	16	0.615385	1	0.5

Table 5
Comparison of Keeling source and Bayesian sources.

locality	Keeling Source (Asare et al., 2025)	Keeling sources mapped to Four Classed Sources	Bayes top source	Bayes top prob	match	confident
Ablekuma Central	Natural gas leak	Fossil Gas Leaks	Fossil Gas Leaks	37.1	TRUE	FALSE
Ablekuma North	Combustion (industrial and domestic)	Combustion/Transport	Fossil Gas Leaks	30.1	FALSE	FALSE
Accra Metropolis	Combustion (industrial and domestic) or road transport	Combustion/Transport	Industrial/Enriched	40.7	FALSE	FALSE
Ada East	Natural gas leak	Fossil Gas Leaks	Fossil Gas Leaks	38.7	TRUE	FALSE
Ada West	Wetlands	Biogenic	Biogenic	66.6	TRUE	TRUE
Adenta	Landfill	Biogenic	Biogenic	56.1	TRUE	TRUE
Ashaiman	Biogenic source	Biogenic	Fossil Gas Leaks	42.6	FALSE	FALSE
Ayawaso Central	Fossil methane source mix	Fossil Gas Leaks	Fossil Gas Leaks	47.6	TRUE	FALSE
Ayawaso North	Natural gas leak	Fossil Gas Leaks	Fossil Gas Leaks	39.7	TRUE	FALSE
Ayawaso West	Fossil methane source mix	Fossil Gas Leaks	Fossil Gas Leaks	42.3	TRUE	FALSE
Ga Central	Biogenic source	Biogenic	Fossil Gas Leaks	49.0	FALSE	FALSE
Ga East	Fossil methane source mix	Fossil Gas Leaks	Fossil Gas Leaks	45.1	TRUE	FALSE
Ga West	Fossil methane source mix	Fossil Gas Leaks	Fossil Gas Leaks	47.0	TRUE	FALSE
Ga South	Landfill	Biogenic	Biogenic	58.3	TRUE	TRUE
Korle Klottey	Fossil methane source mix	Fossil Gas Leaks	Fossil Gas Leaks	41.4	TRUE	FALSE
Kpone Katamanso	Road transport	Combustion/Transport	Combustion/ Transport	39.9	TRUE	FALSE
Krowor	Combustion (industrial and domestic) or road transport	Combustion/Transport	Fossil Gas Leaks	27.1	FALSE	FALSE
La Dade-Kotopon	Fossil methane source mix	Fossil Gas Leaks	Fossil Gas Leaks	35.4	TRUE	FALSE
La-Nkwantanang-Madina	Natural gas leak	Fossil Gas Leaks	Fossil Gas Leaks	35.6	TRUE	FALSE
Ledzokuku	Combustion (industrial and domestic) or road transport	Combustion/Transport	Industrial/Enriched	37.8	FALSE	FALSE
Ningo Prampram	Biogenic source	Biogenic	Fossil Gas Leaks	43.5	FALSE	FALSE
Okaikwei North	Natural gas leak	Fossil Gas Leaks	Fossil Gas Leaks	38.3	TRUE	FALSE
Shai Osudoku	Combustion (domestic)	Combustion/Transport	Fossil Gas Leaks	28.0	FALSE	FALSE
Tema Metropolis	Combustion (industrial and domestic) or road transport	Combustion/Transport	Industrial/Enriched	47.5	FALSE	FALSE
Tema West	Fossil methane source mix	Fossil Gas Leaks	Fossil Gas Leaks	45.4	TRUE	FALSE
Weija Gbawe	Combustion (domestic) or road transport	Combustion/Transport	Industrial/Enriched	32.0	FALSE	FALSE

sources occupying similar isotopic domains in complex urban settings. For practical prioritization, locality-level posterior probabilities successfully differentiated high-confidence intervention zones from sites requiring additional characterization. Locations with posterior probabilities exceeding 50% for Biogenic attribution (Ada West, Ga South, Adenta) represent immediate candidates for landfill gas capture improvements, while localities showing moderate Fossil Gas Leaks confidence warrant targeted leak detection surveys in industrial corridors. The take-home message is clear: Greater Accra's methane mitigation strategy should prioritize fossil fuel infrastructure leak detection and repair programs alongside improvements to solid waste management, while acknowledging that probabilistic rather than deterministic source attribution is essential when isotopic signatures overlap. This uncertainty-aware framework can guide resource allocation in rapidly urbanizing regions where complete source resolution remains technically challenging. However, because the observations were collected during a single short campaign, the inferred posterior source mix should be interpreted as a campaign-period source attribution; future repeated seasonal and diurnal surveys are needed to determine whether the dominance of fossil gas leakage and the secondary contribution from biogenic sources persist through time.

CRediT authorship contribution statement

Ebenezer Aquisman Asare: Writing – review & editing, Writing – original draft, Visualization, Validation, Supervision, Software, Resources, Methodology, Investigation, Formal analysis, Data curation, Conceptualization. **Dickson Abdul-Wahab:** Writing – review & editing, Writing – original draft, Methodology, Investigation, Formal analysis, Data curation.

Consent for publication

Not applicable.

Ethical approval and consent to participate

This paper was designed and written at the National Nuclear Research Institute, Ghana Atomic Energy Commission, Legon-Accra All the images in this research were originally designed by the authors.

Funding

This research received no funding.

Declaration of competing interest

The authors declare that they have no known competing financial interests or personal relationships that could have appeared to influence the work reported in this paper.

Acknowledgement

The authors acknowledge the contribution of colleagues from the Nuclear Chemistry and Environmental Research Centre, National Nuclear Research Institute (NNRI), Ghana Atomic Energy Commission (GAEC), Box LG 80, Legon-Accra, Ghana.

Appendix A. Detailed description of the mobile CRDS system, discrete plume sampling, laboratory δ^2H-CH_4 analysis, and quality assurance procedures

A.1. Analytical scope

Methane was characterised using methane mole fraction (CH_4, ppm) together with stable isotope information incorporated into an isotope-informed source-apportionment framework. Stable isotope composition was expressed in conventional delta notation (δ, ‰), where carbon-isotope ratios were referenced to Vienna Pee Dee Belemnite (VPDB) and hydrogen-isotope ratios were referenced to Vienna Standard Mean Ocean Water (VSMOW). In the present study, two complementary analytical routes were used. Continuous mobile measurements provided CH_4 mole fraction and δ^{13}C-CH_4, whereas δ^2H-CH_4 was determined subsequently from discrete air/plume samples collected during the field campaign and analysed in the laboratory.

A.2. Mobile CRDS platform for CH_4 and δ^{13}C-CH_4

Continuous mobile measurements were acquired using a vehicle-mounted cavity ring-down spectroscopy (CRDS) isotopic analyser (Picarro G2201-i). The G2201-i is a field-deployable analyser designed for carbon-isotope measurements in methane and carbon dioxide, and in this study, it was used for real-time CH_4 mole-fraction and δ^{13}C-CH_4 observations during road-based plume screening. The instrument was operated as a continuous flow-through system within the survey vehicle, with ambient air sampled through a roof-mounted inlet. According to the manufacturer, the analyser operates in CO_2-only, CH_4-only, or simultaneous CO_2-CH_4 modes, and in combined mode the measurements are interleaved every few seconds. Manufacturer specifications also report a typical sample flow of approximately 25 sccm, a measurement interval on the order of a few seconds, and a typical 10–90% rise/fall response time of approximately 30 s.

The CRDS platform was selected because it provides spatially continuous methane screening with simultaneous δ^{13}C-CH_4 capability, allowing elevated plumes to be recognised in real time during mobile surveys. However, the G2201-i does not directly measure δ^2H-CH_4; therefore hydrogen-isotope information was obtained through a separate offline analytical route based on discrete field sample collection and later laboratory IRMS analysis.

A.3. Mobile survey configuration and field operation

Mobile measurements were undertaken across the study area using road-based transects designed to intercept diverse methane source environments, including dense urban sectors, transport corridors, industrial zones, waste-disposal areas, wetland-influenced environments, and peri-urban settlements. The analyser was installed inside the vehicle and operated continuously while the vehicle traversed pre-planned and adaptive routes. Real-time CH_4 and δ^{13}C-CH_4 output was monitored during the survey so that elevated methane plumes could be identified immediately. When methane enhancements were detected, the field team could slow, loop, or briefly stop at safe locations to improve plume characterization. These plume encounters were also used to guide collection of discrete air/plume samples for subsequent δ^2H-CH_4 analysis. This strategy preserved the high

spatial coverage of mobile CRDS while enabling the additional isotopic constraint provided by hydrogen isotopes.

A.4. Discrete field sampling for later δ^2H-CH_4 analysis

Because δ^2H-CH_4 was not obtainable directly from the mobile CRDS instrument, discrete whole-air samples were collected during the mobile survey from selected plume intervals or methane-enhanced localities. Sampling targeted periods of sustained CH_4 elevation above background so that sufficient methane mass would be available for laboratory hydrogen-isotope analysis. Samples were collected in gas-tight canisters suitable for trace-gas isotope work, labelled in the field, and linked to the corresponding survey interval, locality, date, time, and field notes. Where stronger methane plumes were encountered, smaller sample containers were adequate; where enhancements were weaker, larger sample volumes were collected to ensure sufficient methane for laboratory preconcentration and isotopic analysis. After field collection in Ghana, selected plume samples were preserved in gas-tight sample containers and transported under gas-tight conditions to Greenhouse Gas Laboratory, Department of Earth Sciences, Royal Holloway, University of London, Egham, United Kingdom, for methane preconcentration, chromatographic purification, and δ^2H-CH_4 analysis by pyrolysis-IRMS.

A.5. Laboratory determination of δ^2H-CH_4

After field collection, discrete air/plume samples were transported to the laboratory for methane purification and isotope analysis. Laboratory analysis followed established atmospheric methane isotope procedures based on methane preconcentration, chromatographic purification, and continuous-flow isotope-ratio mass spectrometry (IRMS). In this workflow, methane was first isolated from bulk air by preconcentration, then separated from co-occurring gases and potential interferents by gas chromatography. For δ^2H-CH_4 analysis, purified methane was converted quantitatively to H_2 by high-temperature pyrolysis prior to IRMS measurement. Where carbon-isotope confirmation was required on the same or parallel laboratory samples, methane was combusted quantitatively to CO_2 and analysed by IRMS for δ^{13}C-CH_4.

A.6. Calibration and traceability

A multi-level calibration strategy was applied to ensure traceability and comparability across the field and laboratory components of the campaign. For the mobile CRDS measurements, methane concentration calibration was anchored to certified reference standards traceable to the WMO/NOAA CH_4 scale and spanning the concentration range encountered during mobile sampling. Working standards were normalised by bracketing to confirm concentration linearity across the calibrated domain, with linearity maintained at high agreement across the operational range ($R^2 > 0.999$).

For the isotopic component of the CRDS workflow, primary reference materials traceable to Vienna Pee Dee Belemnite (VPDB) were used to define the δ^{13}C-CH_4 scale. Working standards were normalised using a multi-point calibration approach to minimise scale compression and isotopic bias during field deployment. Routine standard analyses were used to verify that the instrument remained within acceptable performance limits during the survey. For the laboratory isotope analysis, scale normalisation followed standard IRMS practice, with δ^{13}Creferenced to VPDB and δ^2H referenced to Vienna Standard Mean Ocean Water (VSMOW). Laboratory reference materials and working standards were used to control instrumental drift, bracket sample composition, and verify repeatability over analytical runs.

A.7. Quality assurance and quality control

Quality assurance for the CRDS component included routine zero/background checks, periodic analysis of reference gases, verification of concentration linearity, and post-acquisition screening of unstable intervals. The manufacturer's specifications for the G2201-i indicate that the analyser is capable of field deployment and provides concentration and isotopic data at a cadence suitable for plume screening but also note application limitations for real-time vehicular leak pinpointing while driving. Accordingly, the CRDS data were used primarily for plume detection, locality screening, and δ^{13}C-informed characterization rather than as a stand-alone hydrogen-isotope platform. Quality assurance for the laboratory δ^2H-CH_4 analysis included methane preconcentration under controlled laboratory conditions, chromatographic separation from air matrix components, bracketed analysis against appropriate standards, and rejection of samples that failed analytical acceptance criteria. Only isotope results meeting predefined precision and quality-control requirements were retained for final interpretation. This screening step was particularly important for weak plumes and low-concentration samples, where insufficient methane recovery or unstable chromatographic separation can degrade hydrogen-isotope precision.

A.8. Time resolution, response characteristics, and practical detection considerations

The mobile CRDS system produced near-continuous CH_4 and δ^{13}C-CH_4 observations with updates every few seconds, allowing plume-scale methane variability to be tracked spatially during vehicle transects. Manufacturer specifications for the G2201-i report a measurement interval on the order of a few seconds, a typical sample flow of approximately 25 sccm, and a typical 10–90% rise/fall response time of approximately 30 s. These characteristics are appropriate for mobile plume screening and spatial methane reconnaissance, although effective field response also depends on vehicle speed, inlet residence time, and atmospheric dispersion. Under campaign conditions, measurement performance for the mobile system was on the order of ± 0.05ppm (expanded, $k = 2$) for CH_4 and approximately ± 0.3‰ (1σ) for $\delta^{13}C - CH_4$. Because the instrument was used in a mobile field-screening context rather than as a fixed laboratory analyser, performance was evaluated primarily through response characteristics, calibration conformity, check-standard stability, and uncertainty propagation, rather than by assigning a single universal field-wide detection limit. For δ^2H-CH_4, analytical sensitivity was governed not by the CRDS instrument but by the amount of methane recovered from discrete field samples and by the performance of the laboratory preconcentration–IRMS system. In practical terms, low-background air is less suitable for hydrogen-isotope analysis than methane-enhanced plume samples unless large air volumes are collected. The field protocol therefore prioritized methane-enhanced plumes and locality intervals for discrete sampling. Analytical usability of the resulting δ^2H-CH_4 data was determined by methane recovery, chromatographic separation, standard bracketing, and repeatability criteria rather than by a single fixed field detection threshold.

A.9. Data linkage and construction of the final isotope dataset

The final isotope dataset was assembled by linking continuous mobile CRDS observations with laboratory-derived δ^2H-CH_4 results from matched field samples. Each accepted discrete sample was assigned to its corresponding plume or locality using time, position, and field records. The resulting integrated dataset therefore comprised: (i) CH_4 mole fraction and δ^{13}C-CH_4 measured continuously by mobile CRDS; and (ii) δ^2H-CH_4 measured offline by laboratory IRMS from discrete field samples collected during the same campaign. These data were then aggregated into analysis units suitable for source apportionment.

A.10. Uncertainty treatment

Observation-level uncertainty was retained as far as possible throughout both the field and laboratory workflows. For the CRDS component, uncertainty reflected instrument performance, calibration conformity, and data-screening outcomes for CH_4 and δ^{13}C-CH_4. For the laboratory component, uncertainty reflected standardisation, chromatographic separation quality, methane recovery, and IRMS measurement reproducibility for δ^2H-CH_4. Rather than replacing these differences with a single common error term, the analysis retained the uncertainty structure of the observations so that stronger measurements exerted tighter constraint in the Bayesian model, while weaker measurements contributed more diffusely.

Appendix B. Notation summary for the Hierarchical Bayesian dual-isotope mixing model

This appendix summarises the notation used in Eqs. (5)–(19) of the Hierarchical Bayesian methane source-apportionment model. It is included to improve clarity, interpretability, and reproducibility by defining the indices, latent variables, observed quantities, prior parameters, and uncertainty terms used throughout the model formulation. The Bayesian framework estimates source contributions to atmospheric methane observations using methane mole fraction, dual-isotope information $(\delta^{13}C - CH_4)$ and $(\delta^2H - CH_4)$, optional source–receptor weighting, and inventory-informed prior information. Because the model is hierarchical and compositional, several latent terms are introduced to ensure that source fractions remain positive and sum to one while still permitting efficient posterior inference. For ease of reference, the notation is first summarized in Table B1 and then briefly interpreted equation-by-equation.

Table B1
Definitions of symbols used in the Bayesian source-apportionment framework.

Symbol	Definition	Notes / interpretation
$i = 1,\ldots,N$	Index for samples or observation instances	Used for individual methane and isotope observations
$s = 1,\ldots,S$	Index for source classes	In this study, S denotes the reduced set of aggregated methane source classes
$r = 1,\ldots,S$	Auxiliary source index	Used in summations over source classes
$j = 1,\ldots,K$	Index for member sources within an aggregated class	Used when several detailed source categories are pooled into one reduced source class
$k \in \{^{13}C, ^{2}H\}$	Isotope-system index	Refers to $\delta^{13}C - CH_4$ and $\delta^2H - CH_4$
$f_{i,s}$	Fractional contribution of source class s to sample i	Main source-apportionment quantity of interest; constrained to the simplex
$z_{i,s}$	Latent logit-scale parameter associated with $f_{i,s}$	Transformed to valid source fractions using the Softmax function
$p_{0,s}$	Inventory-derived baseline source share for source class s	Obtained by normalising prior inventory emission scalings
$\mu_{z0,s}$	Baseline logit mean for source class s	Derived from $p_{0,s}$
$z_{0,s}$	Baseline latent logit for source class s	Prior-centred on the inventory-informed baseline
σ_{inv}	Standard deviation of the prior on baseline logits	Controls uncertainty around the inventory-informed baseline source shares
σ_{frac}	Standard deviation of the prior on sample-level logits	Controls variation of $z_{i,s}$ around $z_{0,s}$
$M_{i,s}$	Footprint sensitivity or source–receptor weighting linking source s to sample i	Set uniformly when explicit footprint information is unavailable
E_s	Source emission-scaling factor for source class s	Positive, unitless relative source-strength term
E_s^{inv}	Prior inventory emission scaling for source class s	Used to construct $p_{0,s}$
σ_E	Standard deviation of the LogNormal prior on E_s	Controls prior spread in source-strength scaling
$CH_{4,i}^{obs}$	Observed methane mole fraction for sample i	Methane concentration measurement
$\mu_{CH_4,i}$	Modelled methane mole fraction for sample i	Expected methane concentration from the forward model
C_{bg}	Background methane concentration term	Represents non-source-specific background methane
$\overline{CH_4}$	Empirical mean methane concentration	Used to centre the prior on C_{bg}
sd_{CH_4}	Empirical standard deviation of methane concentration	Used to scale methane-related priors
$\delta_i^{k,obs}$	Observed isotopic composition for sample i and isotope system k	Observation-level isotope measurement
$\mu_{\delta^k,i}$	Modelled isotopic composition for sample i and isotope system k	Expected isotope value from the mixing model
δ_s^k	Isotopic signature of source class s for isotope system k	Generic notation for source-specific isotope signatures
μ_s^{13C}	Prior mean $\delta^{13}C - CH_4$ signature for source class s	Inventory- or literature-informed
σ_s^{13C}	Prior standard deviation of $\delta^{13}C - CH_4$ for source class s	Captures within-source variability
μ_s^{2H}	Prior mean $\delta^2H - CH_4$ signature for source class s	Inventory- or literature-informed
σ_s^{2H}	Prior standard deviation of $\delta^2H - CH_4$ for source class s	Captures within-source variability
$\overline{\delta^{13}C}$	Empirical mean $\delta^{13}C - CH_4$	Used where required for prior scaling
$sd_{\delta^{13}C}$	Empirical standard deviation of $\delta^{13}C - CH_4$	Used in weakly informative prior scaling
$\overline{\delta^2H}$	Empirical mean $\delta^2H - CH_4$	Used to summarize the isotope dataset
sd_{δ^2H}	Empirical standard deviation of $\delta^2H - CH_4$	Used in weakly informative prior scaling
K	Number of detailed member sources pooled into one aggregated source class	Used in reduced-source prior construction
μ_j	Mean of the j-th member source prior to aggregation	Used to construct pooled priors
σ_j	Standard deviation of the j-th member source prior to aggregation	Used to propagate within-member uncertainty
$\overline{\mu}$	Aggregated mean for a reduced source class	Derived from pooled member-source statistics
$\overline{\sigma}$	Aggregated standard deviation for a reduced source class	Retains both within-member and between-member uncertainty

(continued on next page)

Table B1 (*continued*)

Symbol	Definition	Notes / interpretation
σ_{CH_4}	Residual standard deviation for the methane likelihood	Observation-model error term for methane
SE_i^k	Observation-level measurement standard error for isotope system k at sample i	Included where available
σ_{model}^k	Residual model-error term for isotope system k	Captures mismatch not explained by reported measurement error
$\sigma_{\text{tot},i}^k$	Total likelihood scale for isotope system k at sample i	Combines SE_i^k and σ_{model}^k

Additional note on compositional constraints

For each sample i, the source fractions satisfy:

$$\sum_{s=1}^{S} f_{i,s} = 1 \tag{20}$$

with

$$0 < f_{i,s} < 1 \tag{21}$$

so that the source-fraction vector lies on the simplex.

Additional note on isotope uncertainty

When observation-level isotope standard errors were available, the total isotope likelihood scale was defined as:

$$\boldsymbol{\sigma}_{\mathbf{tot},i}^{\boldsymbol{k}} = \sqrt{\left(SE_i^k\right)^2 + \left(\sigma_{\text{model}}^k\right)^2} \tag{22}$$

This formulation allows the isotope likelihood to account for both analytical measurement uncertainty and residual model mismatch.

B.1. Brief interpretation of Eqs. (5)–(19)

Eq. (5) defines the footprint matrix $M_{i,s}$ under the simplifying assumption of equal source–receptor weighting where explicit transport information is unavailable.

Eq. (6) defines the expected methane mole fraction $\mu_{CH_4,i}$ as the sum of a background methane term and the source-weighted methane contributions from all source classes.

Eq. (7) defines the expected isotopic composition $\mu_{\delta^k,i}$ through isotopic mass balance, using the source fractions $f_{i,s}$ and the source signatures δ_s^k.

Eq. (8) maps the latent logits $z_{i,s}$ to the simplex, thereby producing valid source fractions $f_{i,s}$ that are positive and sum to one.

Eq. (9) defines the inventory-derived baseline source shares $p_{0,s}$ from the prior source emission scalings E_s^{inv}.

Eq. (10) assigns priors to the baseline logits $z_{0,s}$, centred on the inventory-informed means $\mu_{z0,s}$.

Eq. (11) specifies the sample-level logistic-normal parameterisation for $z_{i,s}$, with dispersion controlled by σ_{frac}. In the present implementation, the diagonal logistic-normal structure was used for computational stability.

Eq. (12) assigns Normal priors to the source isotopic signatures using inventory- or literature-informed means and standard deviations.

Eq. (13) assigns LogNormal priors to the positive source emission scalings E_s.

Eq. (14) defines the pooling of prior means and standard deviations when detailed inventory categories are aggregated into broader source classes, thereby preserving both within-source and between-source uncertainty.

Eq. (15) assigns a Normal prior to the background methane term C_{bg}, centred on a fraction of the empirical methane mean and scaled by observed methane variability.

Eq. (16) specifies the Gaussian likelihood for methane concentration observations.

Eq. (17) specifies the Gaussian likelihood for isotope observations.

Eq. (18) defines the total isotope likelihood scale $\sigma_{\text{tot},i}^k$ by combining observation-level measurement error and residual model error.

Eq. (19) assigns HalfNormal priors to residual standard-deviation terms, scaled using the empirical variability of the corresponding observed channels.

B.2. Interpretive note

The hierarchical Bayesian model should be interpreted as a probabilistic source-apportionment framework in which the source fractions $f_{i,s}$ are posterior distributions rather than fixed deterministic values. Accordingly, posterior means, highest-density intervals, and source-dominance probabilities represent the range of source mixtures that remain plausible given the methane observations, dual-isotope data, prior source information, and the explicit uncertainty structure of the model.

Table B1 is intended to serve as a compact reference for the notation used throughout the Bayesian model formulation, thereby improving clarity, interpretability, and reproducibility of the methane source-apportionment framework.

Data availability

Data will be made available on request.

References

Abril-Pla, O., Andreani, V., Carroll, C., Dong, L., Fonnesbeck, C.J., Kochurov, M., Kumar, R., Lao, J., Luhmann, C.C., Martin, O.A., Osthege, M., Vieira, R., Wiecki, T., Zinkov, R., 2023. PyMC: a modern, and comprehensive probabilistic programming framework in Python. PeerJ Comput. Sci. 9, e1516. https://doi.org/10.7717/peerj-cs.1516.

Asare, E.A., Abdul-Wahab, D., Asamoah, A., Dampare, S.B., Wahi, R., Kaufmann, E.E., Ngaini, Z., Klutse, C.K., Klutse, N.A.B., Buah-Kwofie, A., Omorinoye, O.A., 2025. Methane mapping in Greater Accra: isotopic signatures and mobile detection techniques in a developing urban landscape. Sustain. Chem. One World 5 (December 2024), 100036. https://doi.org/10.1016/j.scowo.2024.100036.

Bakkaloglu, S., Lowry, D., Fisher, R.E., Menoud, M., Lanoisellé, M., Chen, H., Röckmann, T., Nisbet, E.G., 2022. Stable isotopic signatures of methane from waste sources through atmospheric measurements. Atmos. Environ. 276, 119021. https://doi.org/10.1016/j.atmosenv.2022.119021.

Berezina, E., Vasileva, A., Moiseenko, K., Pankratova, N., Skorokhod, A., Belikov, I., Belousov, V., 2023. Atmospheric CH4 and its isotopic composition (δ13C) in urban environment in the example of Moscow, Russia. Atmosphere 14 (5), 830. https://doi.org/10.3390/atmos14050830.

Bockarie, A.S., Marais, E.A., Mackenzie, A.R., 2020. Air pollution and climate forcing of the charcoal industry in Africa. Environ. Sci. Technol. 54 (21), 13429–13438. https://doi.org/10.1021/acs.est.0c03754.

Brownlow, R., Lowry, D., Fisher, R.E., France, J.L., Lanoisellé, M., White, B., Wooster, M. J., Zhang, T., Nisbet, E.G., 2017. Isotopic ratios of tropical methane emissions by atmospheric measurement. Glob. Biogeochem. Cycles 31 (9), 1408–1419. https://doi.org/10.1002/2017GB005689.

Cheewaphongphan, P., Chatani, S., Saigusa, N., 2019. Exploring gaps between bottom-up and top-down emission estimates based on uncertainties in multiple emission inventories: a case study on CH4 emissions in China. Sustainability 11 (7), 2054. https://doi.org/10.3390/su11072054.

Chen, D., Liu, Y., Niu, Z., Wang, A., Otwil, P., Huang, Y., Sun, Z., Pang, X., Zhan, L., Yu, L., 2025. Isotopic signatures of methane emission from oil and natural gas plants in southwestern China. Atmos. Chem. Phys. 25 (18), 11407–11422. https://doi.org/10.5194/acp-25-11407-2025.

Douglas, P.M.J., Stratigopoulos, E., Park, J., Phan, D., 2020. Global Geographic Variability in Freshwater Methane Hydrogen Isotope Ratios and Its Implications for Emissions Source Apportionment and Microbial Biogeochemistry. https://doi.org/10.5194/bg-2020-410.

Elguindi, N., Granier, C., Stavrakou, T., Darras, S., Bauwens, M., Cao, H., Chen, C., Denier van der Gon, H.A.C., Dubovik, O., Fu, T.M., Henze, D.K., Jiang, Z., Keita, S., Kuenen, J.J.P., Kurokawa, J., Liousse, C., Miyazaki, K., Müller, J.-F., Qu, Z., Zheng, B., 2020. Intercomparison of magnitudes and trends in anthropogenic surface emissions from bottom-up inventories, top-down estimates, and emission scenarios. Earth's Future 8 (8). https://doi.org/10.1029/2020EF001520.

Environmental Protection Agency (EPA), 2022. Ghana's fifth national greenhouse gas inventory (issue May). www.epa.gov.gh.

Fiehn, A., Eckl, M., Kostinek, J., Gałkowski, M., Gerbig, C., Rothe, M., Röckmann, T., Menoud, M., Maazallahi, H., Schmidt, M., Korbeń, P., Nęcki, J., Stanisavljević, M., Swolkień, J., Fix, A., Roiger, A., 2023. Source apportionment of methane emissions from the upper Silesian Coal Basin using isotopic signatures. Atmos. Chem. Phys. 23 (24), 15749–15765. https://doi.org/10.5194/acp-23-15749-2023.

France, J.L., Cain, M., Fisher, R.E., Lowry, D., Allen, G., O'Shea, S.J., Illingworth, S., Pyle, J., Warwick, N., Jones, B.T., Gallagher, M.W., Bower, K., Le Breton, M., Percival, C., Muller, J., Welpott, A., Bauguitte, S., George, C., Hayman, G.D., Nisbet, E.G., 2016. Measurements of δ13C in CH4 and using particle dispersion modeling to characterize sources of arctic methane within an air mass. J. Geophys. Res. 121 (23), 14,257–14,270. https://doi.org/10.1002/2016JD026006.

van der Gon, H.D., Beevers, S., D'Allura, A., Finardi, S., Honoré, C., Kuenen, J., Perrussel, O., Radice, P., Theloke, J., Uzbasich, M., Visschedijk, A., 2011. Discrepancies Between Top-Down and Bottom-Up Emission Inventories of Megacities: The Causes and Relevance for Modeling Concentrations and Exposure, pp. 199–204. https://doi.org/10.1007/978-94-007-1359-8_34.

Jacques, C., Sapart, C.J., Fripiat, F., Carnat, G., Zhou, J., Delille, B., Röckmann, T., van der Veen, C., Niemann, H., Haskell, T., Tison, J.L., 2021. Sources and sinks of methane in sea ice: insights from stable isotopes. Elementa 9 (1). https://doi.org/10.1525/elementa.2020.00167.

Lu, X., Harris, S.J., Fisher, R.E., France, J.L., Nisbet, E.G., Lowry, D., Röckmann, T., Van Der Veen, C., Menoud, M., Schwietzke, S., Kelly, B.F.J., 2021. Isotopic signatures of major methane sources in the coal seam gas fields and adjacent agricultural districts, Queensland, Australia. Atmos. Chem. Phys. 21 (13), 10527–10555. https://doi.org/10.5194/acp-21-10527-2021.

Maher, D.T., Santos, I.R., Tait, D.R., 2014. Mapping methane and carbon dioxide concentrations and δ13c values in the atmosphere of two Australian coal seam gas fields. Water Air Soil Pollut. 225 (12), 2216. https://doi.org/10.1007/s11270-014-2216-2.

Meister, P., Wiedling, J., Lott, C., Bach, W., Kuhfuß, H., Wegener, G., Böttcher, M.E., Deusner, C., Lichtschlag, A., Bernasconi, S.M., Weber, M., 2018. Anaerobic methane oxidation inducing carbonate precipitation at abiogenic methane seeps in the Tuscan archipelago (Italy). PLoS One 13 (12), e0207305. https://doi.org/10.1371/journal.pone.0207305.

Menoud, M., Van Der Veen, C., Necki, J., Bartyzel, J., Szénási, B., Stanisavljević, M., Pison, I., Bousquet, P., Röckmann, T., 2021. Methane (CH4) sources in Krakow, Poland: insights from isotope analysis. Atmos. Chem. Phys. 21 (17), 13167–13185. https://doi.org/10.5194/acp-21-13167-2021.

Menoud, M., van der Veen, C., Maazallahi, H., Hensen, A., Velzeboer, I., van den Bulk, P., Delre, A., Korben, P., Schwietzke, S., Ardelean, M., Calcan, A., Etiope, G., Baciu, C., Scheutz, C., Schmidt, M., Röckmann, T., 2022. CH4 isotopic signatures of emissions from oil and gas extraction sites in Romania. Element. Sci. Anthrop. 10 (1). https://doi.org/10.1525/elementa.2021.00092.

Meyer, A.G., Lindenmaier, R., Heerah, S., Benedict, K.B., Kort, E.A., Peischl, J., Dubey, M.K., 2022. Using multiscale ethane/methane observations to attribute coal mine vent emissions in the San Juan Basin from 2013 to 2021. J. Geophys. Res. Atmos. 127 (18). https://doi.org/10.1029/2022JD037092.

Ministry of Environment Science Technology and Innovation (MESTI), 2021. Ghana: Updated Nationally Determined Contribution under the Paris Agreement (2020−2030). In: Environmental Protection Agency (EPA) and the Ministry of Environment, Science, Technology and Innovation (MESTI) (Issue September). https://www4.unfccc.int/sites/ndcstaging/PublishedDocuments/Ghana_First/Ghana%27s_Updated_Nationally_Determined_Contribution_to_the_UNFCCC_2021.pdf.

Python Software Foundation, 2021. *Python [Computer software]* (3.9). https://www.python.org/.

Ramsden, A.E., Ganesan, A.L., Western, L.M., Rigby, M., Manning, A.J., Foulds, A., France, J.L., Barker, P., Levy, P., Say, D., Wisher, A., Arnold, T., Rennick, C., Stanley, K.M., Young, D., O'Doherty, S., 2022. Quantifying fossil fuel methane emissions using observations of atmospheric ethane and an uncertain emission ratio. Atmos. Chem. Phys. 22 (6), 3911–3929. https://doi.org/10.5194/acp-22-3911-2022.

Sun, J., Haghnegahdar, M.A., Fernandez, J.M., Magen, C., Farquhar, J., 2025. Controls on concentrations and clumped isotopologues of vehicle exhaust methane. PLoS One 20 (2 February), e0315304. https://doi.org/10.1371/journal.pone.0315304.

Townsend-Small, A., Marrero, J.E., Lyon, D.R., Simpson, I.J., Meinardi, S., Blake, D.R., 2015. Integrating source apportionment tracers into a bottom-up inventory of methane emissions in the Barnett shale hydraulic fracturing region. Environ. Sci. Technol. 49 (13), 8175–8182. https://doi.org/10.1021/acs.est.5b00057.

Zazzeri, G., Lowry, D., Fisher, R.E., France, J.L., Lanoisellé, M., Grimmond, C.S.B., Nisbet, E.G., 2017. Evaluating methane inventories by isotopic analysis in the London region. Sci. Rep. 7 (1), 4854. https://doi.org/10.1038/s41598-017-04802-6.